

Determining the Dielectric Constant of Solid/Liquid Interfaces

Somaiyeh Dadashi¹, Narendra M. Adhikari², Hao Li¹, Stefan M. Piontek¹, Zheming Wang², Kevin M. Rosso², Eric Borguet^{1*}
¹*Department of Chemistry, Temple University, Philadelphia, PA 19122, USA*
²*Pacific Northwest National Laboratory, Richland, WA 99354, USA*

The dielectric constant (ϵ') of interfacial water is an important parameter, but its measurement has posed challenges, and no consensus has been reached on a generalized expression. We derived a formula for ϵ' of a buried interface using the slab model for a half-solvated sphere: $\epsilon' = \epsilon_1\epsilon_2(\epsilon_2 - \epsilon_1 + 6)/2(2\epsilon_2 + \epsilon_1)$, where ϵ_1 and ϵ_2 are the dielectric constants of the solid and liquid phases, respectively. We experimentally validated this expression using vibrational sum frequency generation and Fresnel factor calculations for interfaces of alumina with water (H_2O and D_2O) and acetonitrile. This fills an important knowledge gap in the description of the dielectric constant of interfaces.

Introduction.— The unique properties of liquids at interfaces or under confinement arise from asymmetric forces and molecular interactions that differ from those in bulk [1, 2]. Notably, the reduced rotational freedom of water dipoles near surfaces can lead to a decrease in the dielectric constant at the interface [3, 4], influencing surface interactions, mass transport, ionic adsorption [5], and chemical equilibria [6], which in turn impact atmospheric chemistry [7–9] as well as various chemical and biological processes [10, 11]. For example, the interfacial electric fields, which according to Coulomb’s law inversely depend on the interfacial dielectric constant, are believed to be the driving force of the high activity of interfacial water environments in “on-droplet” chemistry [12, 13]. Therefore, understanding the dielectric constant of the interface is crucial due to its significant contributions to many interfacial phenomena [1, 14–17].

Multiple experimental and theoretical approaches [18], including plasmonic sensors [19], atomic force microscopy [3, 14, 20], and classical molecular dynamics (MD) simulations of water in charged nanopores [21], have been employed to investigate the static and optical dielectric constants of water in interfacial regions or confined environments. For example, the value of the static dielectric constant at the air/water interface has been reported to be ~ 2 [20]. Additionally, local capacitance measurements have shown that the 2-3 layers of water confined between thin channels of hexagonal boron nitride crystals have an out-of-plane dielectric constant of ~ 2 [3]. There is qualitative agreement that these values are significantly smaller compared to the bulk water static dielectric constant of ~ 80 , and above its value of ~ 1.8 at optical frequencies [3, 14, 20].

The dielectric constant, a frequency dependent quantity, has four distinct components: ionic transport, dipole reorientation, vibrational and electronic resonances [22]. Under confinement or at interfaces, the reorientation of molecules is likely reduced so that vibrational and electronic responses should dominate the dielectric function

[3]. Surface specific techniques, e.g., vibrational sum frequency generation (vSFG) spectroscopy, whose response depends on the dielectric constant of the medium, should be sensitive to the interfacial dielectric constant [14, 15]. For example, the vSFG response is inherently sensitive to the interfacial dielectric environment, as the local dielectric function governs the strength of the electromagnetic fields (via Fresnel factors) at the interface [23]. Consequently, the vSFG spectra can yield insight into the interfacial dielectric constant.

The dielectric constant at the air/water interface has been modeled considering the inhomogeneous interfacial dielectric profile using the Lorentz and the slab models [15, 24]. The Lorentz model assumes that the chromophores are completely solvated, resulting in $\epsilon^* = \epsilon(\epsilon^*$: interfacial dielectric constant and ϵ : dielectric constant of water) [25]. The slab model, on the contrary, assumes that the interfacial molecules are partially solvated and treated as idealized hemispheres, leading to $\epsilon^* = \epsilon(\epsilon + 5)(4\epsilon + 2)$ for the air/liquid interface [26]. Both models are commonly used for liquid/vapor interfaces, where the dielectric constant of air is 1, and ϵ' is largely determined by the liquid medium’s dielectric constant. However, whether these formulas for the dielectric constant accurately describe the environment at buried, e.g., solid/liquid, interfaces is not clear.

We derived expressions for ϵ' for the solid/liquid interface based on the slab and Lorentz models. We then devised an approach to test their validity through angle-dependent vSFG spectroscopy and Fresnel factor calculations using the $\alpha\text{-Al}_2\text{O}_3(0001)$ surface in contact with H_2O , D_2O , and acetonitrile. The results showed that the slab model more accurately estimates the interfacial dielectric constant. We further compared the angle-dependent Fresnel factors using distinct ϵ' models, which enabled us to determine the interfacial dielectric constant, ϵ' . Our calculations, confirmed by our experiments, suggest that ϵ' can be defined using the expression that we derive for buried interfaces, $\epsilon' = \epsilon_1\epsilon_2(\epsilon_2 - \epsilon_1 + 6)/2(2\epsilon_2 + \epsilon_1)$ where ϵ_1 and ϵ_2 are the dielectric constants of solid and liquid phase, respectively, which generalizes the approach of Shen *et al.* [26]. Although the majority of models discussed in the liter-

* Correspondence email address: eborguet@temple.edu

ature were not effective in estimating the interfacial dielectric constant, one formula, derived from classical MD simulation [27], shows good agreement with our expression for ϵ' , which further supports its validity.

Experimental methods.— Details of experiments, including sample preparation, optical setup, spectrum normalization and other information, can be found in the Supplemental Material section I and II.

Results and discussion.— Expressions for the dielectric constant of the interfacial region, ϵ' , have been determined by several different approaches [27, 28]. Morita *et al.* used classical MD simulations to determine an expression, $(0.8\sqrt{\epsilon_2} + 0.2\sqrt{\epsilon_1})^2$, for the interfacial dielectric constant of the vapor (ϵ_1)/liquid (ϵ_2) interface [27]. Shen *et al.* derived an expression, $\epsilon^* = \epsilon_2(\epsilon_2 + 5)/(4\epsilon_2 + 2)$, using the slab model to calculate local-field corrections for the monolayer/air interface [26]. The applicability of ϵ^* expression to buried, e.g., solid/liquid, interfaces remains unexplored and debatable. For example, at solid/liquid interfaces, where the solid phase, such as Al_2O_3 , has a higher dielectric constant (ϵ_1), with $\epsilon \approx 2.9$ at 3350 cm^{-1} , compared to the liquid phase (ϵ_2), e.g., water with $\epsilon = 1.74 + i0.75$, the impact of both ϵ_1 and ϵ_2 must be considered in the calculation of the interfacial dielectric constant [29].

Following classical electrodynamics, we used two approaches, the Lorentz and slab models, to calculate the interfacial dielectric constant [30]. The slab model, which considers a half-solvated shell for molecules at the interface, shows good agreement with our results. The Lorentz model, however, did not show good agreement with the experiments as it overestimated ϵ' when compared to the experimental results (Further information comparing the two approaches can be found in the Supplemental Material section III and IV). We believe the success of the half-solvated model is due to its more accurate representation of interfacial molecules, which, compared to bulk molecules, should lack part of their solvation shell [31, 32]. We used an approach similar to Shen *et al.* [26], who derived an equation for the solid/air interface dielectric constant, to calculate ϵ' at the solid/liquid interface considering that the dielectric constant of the solid medium, (ϵ_1), is more than 1. An external field induces charges on a dielectric sphere (ϵ_1) in a dielectric

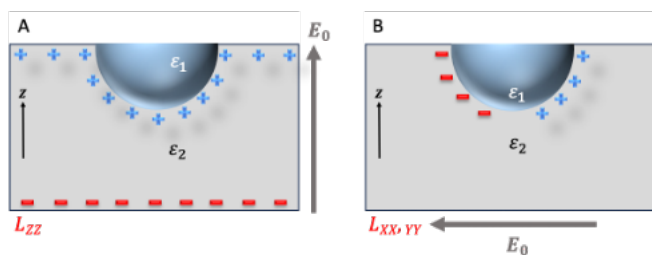


FIG. 1. Schematic representation of the slab model for a hemisphere interacting with an external electric field E_0 along A) the Z-axis and B) the X or Y-axes.

medium of different dielectric constant (ϵ_2) (FIG. 1A), generating an electric field due to the polarization of the medium. As a result, the local electric field is amplified through additional dipole fields generated by the polarization on the sphere in the X, Y and Z directions (FIG. 1A and 1B) [28].

We calculated the induced local fields perpendicular, E_{\perp} FIG.(1A), and parallel, E_{\parallel} (FIG 1B), to the surface using the approach for a dielectric hemisphere of dielectric constant (ϵ_1) in a medium with a different dielectric constant (ϵ_2) [30]. Based on Shen *et al.*, the local field at the interface is the sum of the external field, E_0 , and the field generated through polarization inside the hemisphere, which in our case represents a half solvated molecule, and the surrounding semi-infinite medium [26]. However, due to the isotropic symmetry of the medium, the dipole field originating from the polarization in the bulk is zero [26]. E_{\perp} and E_{\parallel} , can be described using Eq. 1 and Eq. 2 (See Supplemental Material section III for further details):

$$E_{\perp} = E_0 \left(\frac{\epsilon_2 - \epsilon_1 + 3}{3} \right) \quad (1)$$

$$E_{\parallel} = E_0 \left(\frac{2\epsilon_2 + \epsilon_1}{3\epsilon_2} \right) \quad (2)$$

The local field applied to the molecules at the interface, which in our case is the half-solvated hemisphere, is proportional to the external electric field, E_0 . The local fields can be defined through the local electric field correction factors, discussed below in more detail, by knowing the dielectric functions of the media and the interfacial region as well as the angles of incidence of the input laser beams. These correction factors are embedded in the vSFG response, enabling this technique to be used for determining the unknown interfacial dielectric function [33].

Sum frequency generation is a surface-specific second-order nonlinear technique [33, 34]. Within the electric dipole approximation, all second-order processes are forbidden in isotropic media, as the effective second-order susceptibility, $\chi_{\text{eff}}^{(2)}$, vanishes due to symmetry constraints [34]. However, the intrinsically non-centrosymmetric interface results in a non-vanishing $\chi_{\text{eff}}^{(2)}$ that enables the generation of a vSFG response (Eq. 3) [34].

$$I(\omega_{\nu \text{ SFG}}) = \left| \chi_{NR}^{(2)} e^{i\varphi_{NR}} + \sum_{\nu} \frac{A_{\nu}}{\omega_{\text{IR}} - \omega_{\nu} + i\Gamma_{\nu}} \right|^2 I_{\text{vis}} I_{\text{IR}} \quad (3)$$

where A_{ν} is the amplitude, Γ_{ν} is the damping coefficient, ω_{ν} represents the central frequency of the (ν_{th} vibrational mode), and φ_{NR} is the phase of the second order non-resonant ($\chi_{NR}^{(2)}$) nonlinear susceptibilities [28]. The vSFG response can be measured under SSP (S- for vSFG,

S- for visible, and P- for IR), SPS, PSS and PPP polarization combinations, each probing different components of $\chi_{\text{eff}}^{(2)}$ tensor that can be expressed by macroscopic elements $\chi_{IJK}^{(2)}$ (I, J, K = X, Y, Z) through the following equations, Eq. 4a- Eq. 4d, with S referring to s-polarized light and P to p-polarized light, where the electric field is oriented perpendicular and parallel to the plane of incidence, respectively [28, 35].

$$\chi_{\text{eff, SSP}}^{(2)} = L_{YY}(\omega_{SFG}) L_{YY}(\omega_{VIS}) L_{ZZ}(\omega_{IR}) \sin \theta_{IR} \chi_{YYZ} \quad (4a)$$

$$\chi_{\text{eff, SPS}}^{(2)} = L_{YY}(\omega_{SFG}) L_{ZZ}(\omega_{VIS}) L_{YY}(\omega_{IR}) \sin \theta_{VIS} \chi_{YZY} \quad (4b)$$

$$\chi_{\text{eff, PSS}}^{(2)} = L_{ZZ}(\omega_{SFG}) L_{YY}(\omega_{VIS}) L_{YY}(\omega_{IR}) \sin \theta_{SFG} \chi_{ZYY} \quad (4c)$$

$$\begin{aligned} \chi_{\text{eff, PPP}}^{(2)} = & -L_{XX}(\omega_{SFG}) L_{XX}(\omega_{VIS}) L_{ZZ}(\omega_{IR}) \\ & \cos \theta_{SFG} \cos \theta_{VIS} \sin \theta_{IR} \chi_{XXX} \\ & - L_{XX}(\omega_{SFG}) L_{ZZ}(\omega_{VIS}) L_{XX}(\omega_{IR}) \\ & \cos \theta_{SFG} \sin \theta_{VIS} \cos \theta_{IR} \chi_{XZX} \\ & + L_{ZZ}(\omega_{SFG}) L_{XX}(\omega_{VIS}) L_{XX}(\omega_{IR}) \\ & \sin \theta_{SFG} \cos \theta_{VIS} \cos \theta_{IR} \chi_{ZXX} \\ & + L_{ZZ}(\omega_{SFG}) L_{ZZ}(\omega_{VIS}) L_{ZZ}(\omega_{IR}) \\ & \sin \theta_{SFG} \sin \theta_{VIS} \sin \theta_{IR} \chi_{ZZZ} \end{aligned} \quad (4d)$$

where θ is the incident angle with respect to the surface normal, and the L_{II} ($I = X, Y, Z$) are the Fresnel factors that describe the local field corrections [34].

When an external electric field is applied to the interface, the medium becomes polarized, consequently altering the electric field at the interface [28]. The Fresnel factors, elements of a 3×3 tensor, are local field correction factors ($L_{II} : L_{XX}, L_{YY}, L_{ZZ}$) that account for changes in the electric fields at interfaces [28]. The Fresnel factors can be calculated (Eq. 5a - Eq. 5c) knowing the dielectric constants of medium 1 (ε_1), medium 2 (ε_2) and the interface (ε') as well as the angles of the incident beams [28]:

$$L_{XX}(\omega_I) = \frac{2\varepsilon_1(\omega_I) \cos \gamma_I}{\varepsilon_1(\omega_I) \cos \gamma_I + \varepsilon_2(\omega_I) \cos \theta_I} \quad (5a)$$

$$L_{YY}(\omega_I) = \frac{2\varepsilon_1(\omega_I) \cos \theta_I}{\varepsilon_1(\omega_I) \cos \theta_I + \varepsilon_2(\omega_I) \cos \gamma_I} \quad (5b)$$

$$L_{ZZ}(\omega_I) = \frac{2\varepsilon_2(\omega_I) \cos \theta_I}{\varepsilon_1(\omega_I) \cos \gamma_I + \varepsilon_2(\omega_I) \cos \theta_I} \frac{\varepsilon_1(\omega_I)}{\varepsilon'(\omega_I)} \quad (5c)$$

where the θ_I represent the angles of incidence for the input beams, and the γ_I are the angles of the transmitted waves calculated using Snell's law [36]. The interfacial dielectric constant is buried in the Fresnel factor,

$L_{ZZ}(\omega_I)$, offering the opportunity to determine the interfacial dielectric constant through angle-dependent vSFG experiments.

The electric field components at the interface, E_{\perp} and E_{\parallel} , can be determined using the Fresnel equations [28]. Knowing that $L_{ZZ}/L_{YY} = \varepsilon_1/\varepsilon'$, $L_{XX} = L_{YY} = E_{\perp}/E_0$ and $L_{ZZ} = E_{\parallel}/E_0$ we have [26] (See Supplemental Material section III and Eq. S13 for further details):

$$\varepsilon' = \frac{\varepsilon_1 \varepsilon_2 (\varepsilon_2 - \varepsilon_1 + 6)}{2(2\varepsilon_2 + \varepsilon_1)} \quad (6)$$

At optical frequencies, we typically use the refractive index as per Maxwell's relation, $n = \sqrt{\varepsilon}$, and therefore [14, 15]:

$$n' = \sqrt{\frac{n_1^2 n_2^2 (n_2^2 - n_1^2 + 6)}{2(n_2^2 + n_1^2)}} \quad (7)$$

To validate the expression that we derived for ε' , we collected angle-dependent vSFG spectra under three different experimental geometries that were selected, considering the critical angles at the solid/liquid interfaces. The vSFG experiments were performed at two total internal reflection (TIR) geometries (i.e., with angle-of-incidence higher than the critical angle for the IR and visible beams at the solid/liquid interface; Table S1 in the Supplemental Material section V), TIR1: $\theta_{\text{vis}} \approx 63^\circ$, $\theta_{\text{IR}} \approx 57^\circ$, TIR2: $\theta_{\text{vis}} \approx 54^\circ$, $\theta_{\text{IR}} \approx 60^\circ$ and in an "external" geometry, where the angles of incidence of the incoming beams are less than the critical angle: $\theta_{\text{vis}} \approx 31^\circ$, $\theta_{\text{IR}} \approx 29^\circ$ (Further details can be found in the Supplemental Material section V). TIR geometries were selected for to improve the signal-to-noise ratio.

We performed vSFG experiments on aqueous/aluminum oxide/ interfaces, due to their abundance and importance in nature [33, 37]. Specifically, we investigated the $\text{H}_2\text{O}/\alpha\text{-Al}_2\text{O}_3(0001)$, and $\text{D}_2\text{O}/\alpha\text{-Al}_2\text{O}_3(0001)$ interfaces in the OH and the OD stretch regions, respectively, as well as the $\text{CH}_3\text{CN}/\alpha\text{-Al}_2\text{O}_3(0001)$ in the C = N stretch and the C - H stretch regions (FIG. 2) interfaces. The vSFG spectra of acetonitrile in the C \equiv N stretch and CH stretch region are similar to previous studies of this solid/liquid interface in that a single feature is observed near $\sim 2250 - 2260 \text{ cm}^{-1}$ (FIG. 2A) and near $2940 - 2950 \text{ cm}^{-1}$ (FIG. 2B) [38-43]. We did not observe the Fermi resonance peak which arises from the coupling between the C \equiv N stretch and the combination band ($\sim 2300 \text{ cm}^{-1}$) of the C - C stretching and C - H bending modes since this mode is expected to lie at the edge of the IR profile used in our experiments [44]. The presence of single narrow peaks in the C \equiv N and the CH stretching spectral regions makes these features effective for benchmarking the dielectric constant at the interface [39?].

As the experimental geometry changes from TIR2 to

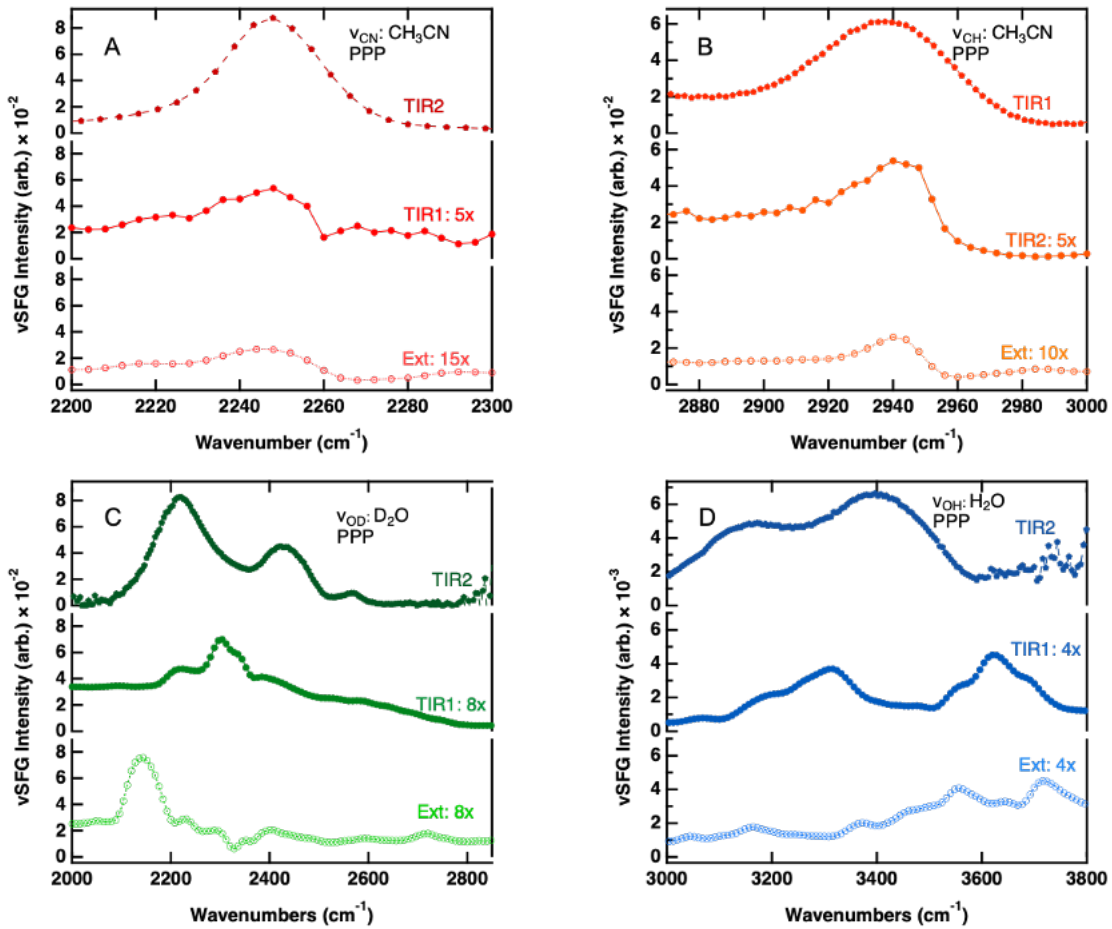


FIG. 2. vSFG spectra for A) C \equiv N stretch of CH₃CN, B) CH stretch of CH₃CN, C) OD stretch of D₂O and the OH stretch of H₂O at α -Al₂O₃(0001) interfaces. All of the experiments were performed using the PPP polarization combination in different geometries, TIR2 (Top), TIR1 (Middle), and Ext. (Bottom) in each panel.

TIR1 and then to the external geometry, $I(\omega_{\nu SFG})$ decreases for the C \equiv N stretch and CH stretch of CH₃CN at liquid/ α -Al₂O₃(0001) interface. The OD stretch D₂O (FIG. 2C) and the OH of H₂O (FIG. 2D) for TIR2 and TIR1 shows distinct peaks for strongly hydrogen bonded (OD \sim 2200 – 2400 cm⁻¹ and OH \sim 3000 – 3400 cm⁻¹) and weakly hydrogen bonded (OD \sim 2400 – 2700 cm⁻¹ and OH \sim 3400 – 3700 cm⁻¹) regions. For the external geometry, we observe an additional, relatively weak peak near \sim 2730 cm⁻¹ for OD stretch (FIG. 2C) and near \sim 3750 cm⁻¹ for OH stretch (FIG. 2D). These OD and OH stretch spectral characteristics suggest that distinct hydrogen bonding environments are probed in the external geometry compared to what is detected in the TIR geometries.

To evaluate ϵ' we compared the experimental ratios of the effective second order nonlinear susceptibility for the PPP polarization combination ($|\chi_{\text{eff}, PPP}^{(2)}|^2$) for TIR2 and TIR1 in relation to the external geometry (FIG. 3) with the calculated values for different spectral regions. These include the C \equiv N stretch (FIG. 3A) and the CH stretch (FIG 3B) of CH₃CN, the OD stretch of D₂O

at 2350 cm⁻¹ (FIG 3C) and the OH stretch of H₂O at 3350 cm⁻¹ (FIG. 3D). Utilizing our expression and six other models for ϵ' (Table S2, Supplemental Material section VI), we calculated the $|\chi_{\text{eff}, PPP}^{(2)}|^2$ ratio for each geometry using Eq. 4d and the Fresnel coefficients of $L_{XX}(\omega_I)$, $L_{YY}(\omega_I)$ and $L_{ZZ}(\omega_I)$ described in Eq. 5a - Eq. 5c. The $|\chi_{\text{eff}, PPP}^{(2)}|^2$ ratio comparison shows that our expression $\epsilon_1\epsilon_2(\epsilon_2 - \epsilon_1 + 6)/2(2\epsilon_2 + \epsilon_1)$ and the expression from MD simulations [27], marked by red arrows in FIG. 3, estimate ϵ' better than other models for a broad range of spectral regions investigated here. By comparing the calculated $|\chi_{\text{eff}, PPP}^{(2)}|^2$ ratio with the experimental values, we showed that all other models underestimated ϵ' by factors of 5 to 10 compared to the experiments. (FIG. S2: Supplemental Material section VI). Additionally, the model using ϵ_2 as ϵ' , i.e., only considering the dielectric constant of the bulk liquid phase, overestimates the interfacial dielectric constant and ignores the impact of the solid on ϵ' . The formula $\epsilon^* = \epsilon_2(\epsilon_2 + 5)/(4\epsilon_2 + 2)$ appears to effectively estimate the interfacial dielectric constant at the air/liquid

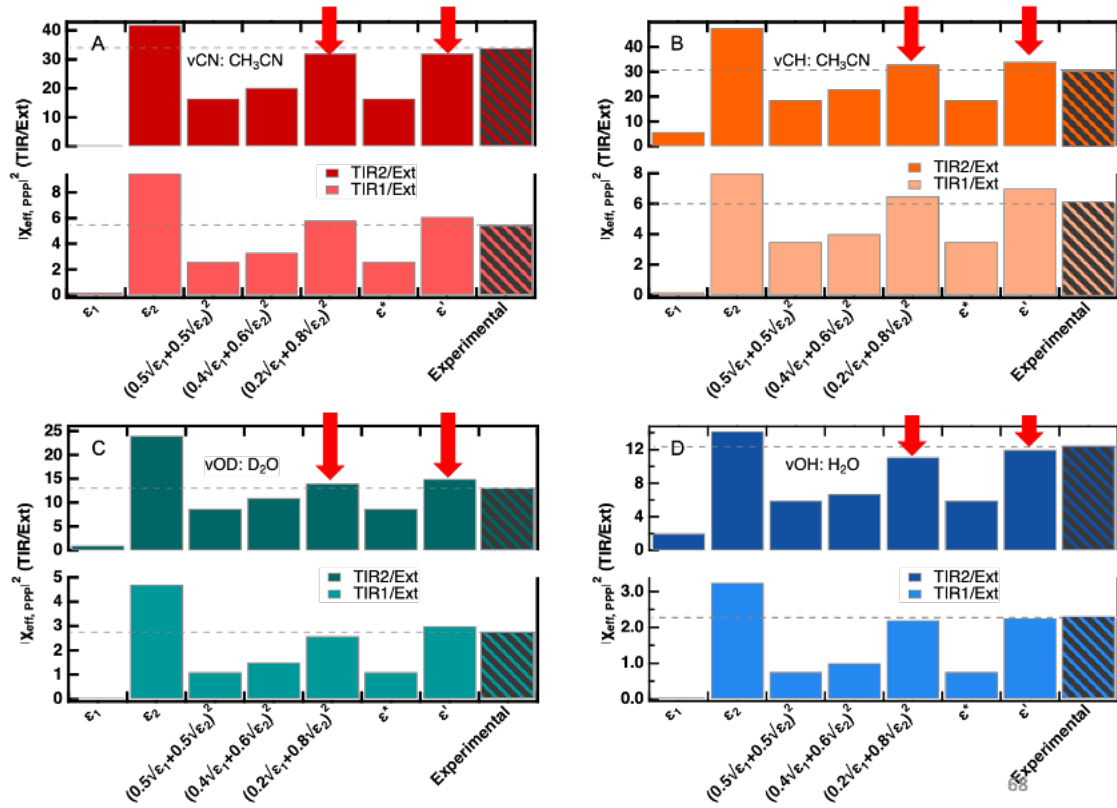


FIG. 3. The ratio of $|\chi_{\text{eff}, PPP}^{(2)}|^2$ of the total internal reflection versus the external reflection geometry for A) C \equiv N stretch of CH₃CN, B) CH stretch of CH₃CN, C) OD stretch of D₂O and, D) the OH stretch of H₂O at the α -Al₂O₃ interfaces. Our expression and six different models for ϵ' including: $\epsilon_1, \epsilon_2, (0.5\sqrt{\epsilon_1} + 0.5\sqrt{\epsilon_2})^2, (0.4\sqrt{\epsilon_1} + 0.6\sqrt{\epsilon_2})^2, (0.2\sqrt{\epsilon_1} + 0.8\sqrt{\epsilon_2})^2, \epsilon^* = \epsilon_2(\epsilon_2 + 5)/(4\epsilon_2 + 2)$ and $\epsilon' = \epsilon_1\epsilon_2(\epsilon_2 - \epsilon_1 + 6)/2(2\epsilon_2 + \epsilon_1)$ compared to the experimental results (last bar on the right). Gray dashed line indicates the experimental value. The top row in each panel refers to TIR2 and the bottom row refers to TIR1.

and air/solid interface [15, 26, 28]. However, our experimental results indicate that $\epsilon^* = \epsilon_2(\epsilon_2 + 5)/(4\epsilon_2 + 2)$ might not be accurate for estimating ϵ' at solid/liquid interfaces because, as shown in FIG. 3 A-D, the $|\chi_{\text{eff}, PPP}^{(2)}|^2$ ratio calculated using this formula is lower than the experimental ratio. This is not surprising since the dielectric constant of the solid is different from that of air.

The vSFG response of water at various mineral interfaces reflects the differences in the hydrogen bonding environment of the first few layers [45]. This diversity in interactions becomes evident when probing the OH and OD stretch region, [45]. It is important to note that the Fresnel factors exhibit a noticeable frequency dependence, primarily driven by the frequency-dependent dielectric constant of bulk water in the infrared region [46].

To further investigate if our expression, $\epsilon' = \epsilon_1\epsilon_2(\epsilon_2 - \epsilon_1 + 6)/2(2\epsilon_2 + \epsilon_1)$, for the interfacial dielectric constant provides consistent results with respect to frequency, we compared the $|\chi_{\text{eff}, PPP}^{(2)}|^2$ for TIR2 and TIR1 versus the external geometry at

different frequencies in the OH and OD stretch regions. The results indicate that our expression provides accurate estimates of the modulus of the interfacial dielectric constant for these frequencies (FIG. 4: A and B). Between the six different expressions, only our expression and the one from classical MD simulations [27], $\epsilon' = (0.2\sqrt{\epsilon_1} + 0.8\sqrt{\epsilon_2})^2$, show good agreement with the experimental results at the OH (FIG. 3A) and OD (FIG. 3B) stretch frequencies (FIG. S9: A and B). Our expression, derived from a continuum electrostatic approach, agrees well with the microscopic approach intrinsic to MD simulations further validates our model.

Using our expression for the interfacial dielectric constant for both OH of H₂O and OD stretching of D₂O reveals that $|\epsilon'|$ shows frequency dependency, as expected, and varies between 1.6-2.4 (FIG. 4C) and 1.8-2.4 (FIG. 4D) at these interfaces, respectively. In addition, $|\epsilon'|$ for H₂O and D₂O at the interface appears higher than their bulk values, which could arise from the influence of Al₂O₃ surface [47]. Our value for the interfacial dielectric constant of H₂O and D₂O, calculated from our expression and corroborated by

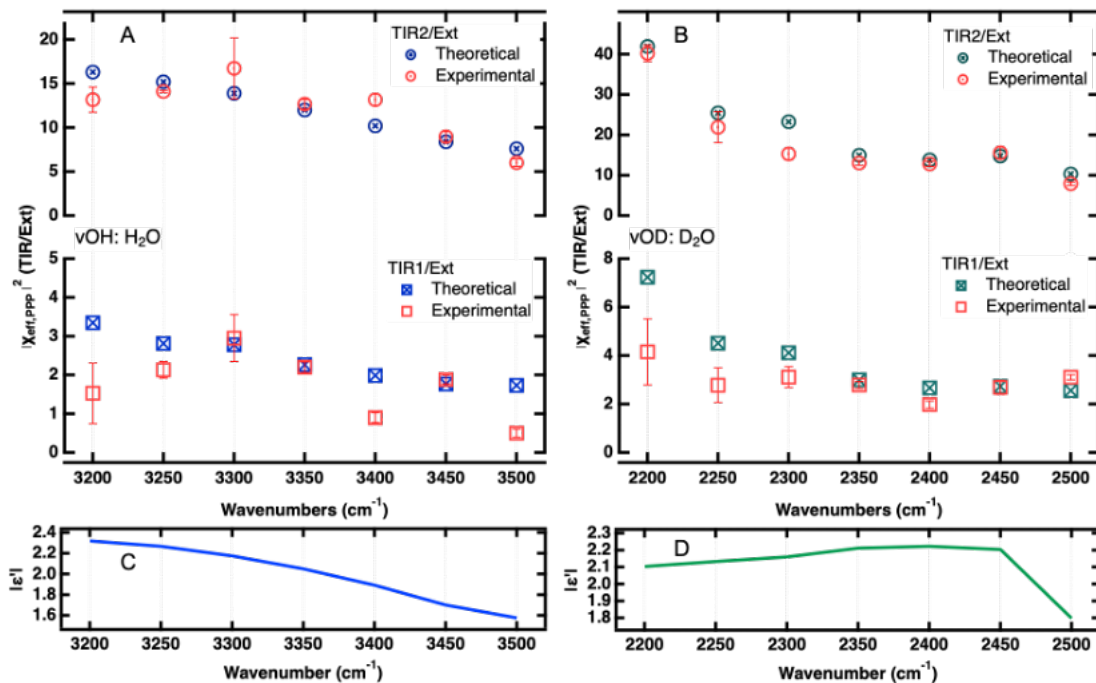


FIG. 4. Calculated frequency dependent $|\chi_{\text{eff},PPP}^{(2)}|^2$ ratio for TIR2 (Top) and TIR1 (Bottom) with respect to the external geometry for the A) OH stretch of H₂O (blue) B) OD stretch of D₂O (green) at the α -Al₂O₃ interfaces compared to the experimental data (red). The dependence of $|\epsilon'|$ at the C) H₂O/ α -Al₂O₃ and the D) D₂O/ α -Al₂O₃ interfaces. The expression $\epsilon' = \epsilon_1\epsilon_2(\epsilon_2 - \epsilon_1 + 6)/2(2\epsilon_2 + \epsilon_1)$, was used to calculate the interfacial dielectric constant.

results from MD simulations (FIG. S9C and D), shows that $|\epsilon'|$ is close to the value of the static dielectric constant ($\epsilon \sim 2$) determined under confinement [3]. Additionally, using our expression we can estimate that $|\epsilon'|$ for the C \equiv N and the CH stretch of CH₃CN are ~ 2.28 and 2.04 , respectively, are higher compared to their bulk values, ~ 1.69 and 1.78 , respectively due to the influence of Al₂O₃ surface [48],

Conclusions.—We have derived a generalized expression for the interfacial dielectric constant at buried, solid/liquid interfaces, $\epsilon' = \epsilon_1\epsilon_2(\epsilon_2 - \epsilon_1 + 6)/2(2\epsilon_2 + \epsilon_1)$, using a slab model for a half-solvated sphere, and employed angle-dependent vSFG spectroscopy and Fresnel factor calculations to evaluate this expression in different infrared spectral regions. We showed that our approach is effective in predicting the interfacial dielectric constant across a broad frequency range for several liquids (H₂O, D₂O and acetonitrile) in contact with Al₂O₃ surfaces. We

expect that our expression will be valid across various other types of buried interfaces which is fundamentally important for heterogeneous chemical reactions like hydrolysis, hydrogenation, and crosscoupling reactions, etc.

Acknowledgements.—EB thanks the National Science Foundation (CHE 2102557) for supporting this work. N.A., Z.W., and K.M.R. were supported by the U.S. Department of Energy (DOE), Office of Science, Office of Basic Energy Sciences, Chemical Sciences, Geosciences and Biosciences Division through its Geosciences program at PNNL (FWP #56674). A portion of the research was performed using EMSL, a DOE Office of Science User Facility sponsored by the Office of Biological and Environmental Research. PNNL is a multi-program national laboratory operated for the DOE by Battelle Memorial Institute under Contract No. DE-AC05-76RL01830.

- [1] P. Sit, *Characterization of Biomaterials* (Woodhead Publishing, 2013).
- [2] K. Eisenthal, Liquid interfaces probed by second-harmonic and sum-frequency spectroscopy, *Chemical Reviews* **96**, 1343 (1996).
- [3] L. Fumagalli, A. Esfandiari, R. Fabregas, S. Hu, P. Ares, and A. J. et al., Anomalously low dielectric constant of

confined water, *Science* **360**, 1339 (2018).

- [4] H. Zhu, F. Yang, Y. Zhu, A. Li, W. He, J. Huang, and G. Li, Investigation of dielectric constants of water in a nano-confined pore, *RSC Advances* **10**, 8628 (2020).
- [5] R. Wang, M. DelloStritto, R. C. Remsing, V. Carnevale, M. L. Klein, and E. Borguet, Sodium halide adsorption and water structure at the α -alumina(0001)/water inter-

- face, *The Journal of Physical Chemistry C* **123**, 15618 (2019).
- [6] E. D. Boyes, A. P. LaGrow, M. R. Ward, R. W. Mitchell, and P. L. Gai, Single atom dynamics in chemical reactions, *Accounts of Chemical Research* **53**, 390 (2020).
- [7] J. L. Jimenez, M. Canagaratna, N. Donahue, A. Prevot, Q. Zhang, and J. H. K. et al., Evolution of organic aerosols in the atmosphere, *Science* **326**, 1525 (2009).
- [8] X. Yu, T. Seki, C.-C. Yu, K. Zhong, S. Sun, and M. O. et al., Interfacial water structure of binary liquid mixtures reflects nonideal behavior, *The Journal of Physical Chemistry B* **125**, 10639 (2021).
- [9] J. Zhong, M. Kumar, J. S. Francisco, and X. C. Zeng, Insight into chemistry on cloud/aerosol water surfaces, *Accounts of Chemical Research* **51**, 1229 (2018).
- [10] F. Deißbeck and S. Wippermann, Dielectric properties of nanoconfined water from ab initio thermopotential molecular dynamics, *Journal of Chemical Theory and Computation* **19**, 1035 (2023).
- [11] B. Bagchi, *Water in biological and chemical processes: from structure and dynamics to function* (Cambridge University Press, 2013).
- [12] J. K. Lee, K. L. Walker, H. S. Han, J. Kang, F. B. Prinz, R. M. Waymouth, H. G. Nam, and R. N. Zare, Spontaneous generation of hydrogen peroxide from aqueous microdroplets, *Proceedings of the National Academy of Sciences* **116**, 19294 (2019).
- [13] H. Xiong, J. K. Lee, R. N. Zare, and W. Min, Strong electric field observed at the interface of aqueous microdroplets, *Physical Chemistry Letters* **11**, 7423 (2020).
- [14] O. Teschke, G. Ceotto, and E. D. Souza, Interfacial water dielectric-permittivity-profile measurements using atomic force microscopy, *Physical Review E* **64**, 011605 (2001).
- [15] K.-Y. Chiang, T. Seki, C.-C. Yu, T. Ohto, J. Hunger, M. Bonn, and Y. Nagata, The dielectric function profile across the water interface through surface-specific vibrational spectroscopy and simulations, *Proceedings of the National Academy of Sciences* **119**, e2204156119 (2022).
- [16] P. Loche, C. Ayaz, A. Wolde-Kidan, A. Schlaich, and R. R. Netz, Universal and nonuniversal aspects of electrostatics in aqueous nanoconfinement, *The Journal of Physical Chemistry B* **124**, 4365 (2020).
- [17] D. Munoz-Santiburcio and D. Marx, Chemistry in nanoconfined water, *Chemical Science* **8**, 3444 (2017).
- [18] H. Xiao, Z. Yang, L. Zhang, D. Feng, F. Zhang, M. Jiang, Q. Sui, and L. Jia, Compositional analysis of cement raw meal by near-infrared (nir) spectroscopy, *Analytical Letters* **52**, 2931 (2019).
- [19] C. Zhan, B.-W. Liu, Z.-Q. Tian, and B. Ren, Determining the interfacial refractive index via ultrasensitive plasmonic sensors, *Journal of the American Chemical Society* **142**, 10905 (2020).
- [20] O. Teschke and E. D. Souza, Water molecule clusters measured at water/air interfaces using atomic force microscopy, *Physical Chemistry Chemical Physics* **7**, 3856 (2005).
- [21] T. R. Underwood and I. C. Bourg, Dielectric properties of water in charged nanopores, *The Journal of Physical Chemistry B* **126**, 2688 (2022).
- [22] M. B. H. Othman, M. R. Ramli, L. Y. Tyng, Z. Ahmad, and H. M. Akil, Dielectric constant and refractive index of poly (siloxane-imide) block copolymer, *Materials & Design* **32**, 3173 (2011).
- [23] Y. Shen, Surface properties probed by second-harmonic and sum-frequency generation, *Nature* **337**, 519 (1989).
- [24] R. Wang, M. L. Klein, V. Carnevale, and E. Borguet, Investigations of water/oxide interfaces by molecular dynamics simulations, *Wiley Interdisciplinary Reviews: Computational Molecular Science* **11**, e1537 (2021).
- [25] A. Morita, *Theory of sum frequency generation spectroscopy*, *Lecture Notes in Chemistry* (Springer, 2018).
- [26] X. Zhuang, P. Miranda, D. Kim, and Y. Shen, Mapping molecular orientation and conformation at interfaces by surface nonlinear optics, *Physical Review B* **59**, 12632 (1999).
- [27] L. Wang, T. Ishiyama, and A. Morita, Theoretical investigation of C – H vibrational spectroscopy. I. modeling of methyl and methylene groups of ethanol with different conformers, *The Journal of Physical Chemistry A* **121**, 6687 (2017).
- [28] K. Shiratori and A. Morita, Molecular theory on dielectric constant at interfaces: A molecular dynamics study of the water/vapor interface, *The Journal of Chemical Physics* **134**, 234705 (2011).
- [29] I. H. Malitson, Refraction and dispersion of synthetic sapphire, *Journal of the Optical Society of America* **52**, 1377 (1962).
- [30] C. Böttcher, *Theory of Electric Polarization* (Elsevier, 1973).
- [31] A. Eftekhari-Bafrooei and E. Borguet, Effect of hydrogen-bond strength on the vibrational relaxation of interfacial water, *Journal of the American Chemical Society* **132**, 3756 (2010).
- [32] D. Lesnicki, Z. Zhang, M. Bonn, M. Sulpizi, and E. H. G. Backus, Surface charges at the CaF₂/water interface allow very fast intermolecular vibrational-energy transfer, *Angewandte Chemie International Edition* **59**, 13116 (2020).
- [33] S. M. Piontek and E. Borguet, Vibrational spectroscopy of geochemical interfaces, *Surface Science Reports* **78**, 100606 (2023).
- [34] H.-F. Wang, L. Velarde, W. Gan, and L. Fu, Quantitative sum-frequency generation vibrational spectroscopy of molecular surfaces and interfaces: lineshape, polarization, and orientation, *Annual Review of Physical Chemistry* **66**, 189 (2015).
- [35] B. Busson, Sum-frequency generation at interfaces: A fresnel story. ii. analytical expressions for multilayer systems, *The Journal of Chemical Physics* **159** (2023).
- [36] J. Löbau and K. Wolfrum, Sum-frequency spectroscopy in total internal reflection geometry: signal enhancement and access to molecular properties, *Journal of the Optical Society of America B* **14**, 2505 (1997).
- [37] J. L. Bañuelos, E. Borguet, G. E. Brown Jr, R. T. Cygan, J. J. DeYoreo, P. M. Dove, M.-P. Gaigeot, F. M. Geiger, J. M. Gibbs, V. H. Grassian, et al., Oxide–and silicate–water interfaces and their roles in technology and the environment, *Chemical Reviews* **123**, 6413 (2023).
- [38] A. Lock and H. Bakker, Temperature dependence of vibrational relaxation in liquid H₂O, *The Journal of Chemical Physics* **117**, 1708 (2002).
- [39] B. Rehl, Z. Li, and J. M. Gibbs, Influence of high pH on the organization of acetonitrile at the silica/water interface studied by sum frequency generation spectroscopy, *Langmuir* **34**, 4445 (2018).
- [40] C. A. Rivera, J. S. Bender, K. Manfred, and J. T. Fourkas, Persistence of acetonitrile bilayers at the inter-

- face of acetonitrile/water mixtures with silica, *The Journal of Physical Chemistry A* **117**, 12060 (2013).
- [41] L. Wang, S. D. Fried, S. G. Boxer, and T. E. Markland, Quantum delocalization of protons in the hydrogen-bond network of an enzyme active site, *Proceedings of the National Academy of Sciences* **111**, 18454 (2014).
- [42] D. Zhang, J. Gutow, K. Eisenthal, and T. Heinz, Sudden structural change at an air/binary liquid interface: Sum frequency study of the air/acetonitrile–water interface, *The Journal of Chemical Physics* **98**, 5099 (1993).
- [43] S. Dadashi, S. Parshotam, B. Mandal, B. Rehl, J. M. Gibbs, and E. Borguet, Influence of charged site density on local electric fields and polar solvent organization at oxide interfaces, *The Journal of Physical Chemistry C* **128**, 9683–9692 (2024).
- [44] B. Dereka, N. H. Lewis, J. H. Keim, S. A. Snyder, and A. Tokmakoff, Characterization of acetonitrile isotopologues as vibrational probes of electrolytes, *The Journal of Physical Chemistry B* **126**, 278 (2021).
- [45] S. Woutersen, U. Emmerichs, H.-K. Nienhuys, and H. J. Bakker, Anomalous temperature dependence of vibrational lifetimes in water and ice, *Physical Review Letters* **81**, 1106 (1998).
- [46] E. H. Backus, N. Garcia-Araez, M. Bonn, and H. J. Bakker, On the role of Fresnel factors in sum-frequency generation spectroscopy of metal–water and metal-oxide–water interfaces, *The Journal of Physical Chemistry C* **116**, 23351 (2012).
- [47] C. Laurent, H. Billiet, and L. D. Galan, On the use of alumina in HPLC with aqueous mobile phases at extreme pH, *Chromatographia* **17**, 253 (1983).
- [48] K. Moutzouris, M. Papamichael, S. C. Betsis, I. Stavrakas, G. Hloupis, and D. Triantis, Refractive, dispersive and thermo-optic properties of twelve organic solvents in the visible and near-infrared, *Applied Physics B* **116**, 617 (2014).
- [49] J. E. Bertie and Z. Lan, Liquid water- acetonitrile mixtures at 25 c: the hydrogen-bonded structure studied through infrared absolute integrated absorption intensities, *The Journal of Physical Chemistry B* **101**, 4111 (1997).

Determining the Dielectric Constant of Solid/Liquid Interfaces

Supplemental Material

Somaiyeh Dadashi¹, Narendra M. Adhikari², Hao Li¹, Stefan M. Piontek¹, Zheming Wang²,
Kevin M. Rosso², Eric Borguet^{1*}

¹Department of Chemistry, Temple University, Philadelphia, PA 19122, USA

²Pacific Northwest National Laboratory, Richland, WA, 99354, USA

Corresponding author: eborguet@temple.edu

Table of Contents

I. Experimental methods (Sample preparation and optical setups):.....	2
a. PNNL.....	2
b. Temple University.....	3
II. Experimental geometries:.....	5
III. Approaches for deriving the interfacial dielectric constant:.....	6
a. The slab model.....	6
b. The Lorentz model	11
IV. Comparison of expressions derived using the slab model (III-a) vs. Lorentz model (III-b):	13
V. Critical angles:	14
VI. Angular dependent effective nonlinear susceptibility $\left \chi_{eff,PPP}^{(2)} \right ^2$ of the TIR2 and TIR1 and the external geometry with constant IR angle:	15
VII. Which expression performs better?	22
VIII. References:.....	25

I. Experimental methods (Sample preparation and optical setups):

a. PNNL

CH₃CN (HPLC Grade, Fisher Scientific Inc.), H₂O (nanopore DI water with a resistivity of 18.1 MΩ.cm), D₂O (99.9 atom % D atoms; Sigma-Aldrich Corp. St. Louis, MO, USA), and double-side polished Al₂O₃(0001) windows, 0.5''x0.5''x0.5mm (MTI Corporation, Richmond, CA, USA) were used for the experiments. Before the vibrational sum frequency generation (vSFG) measurements, the alumina windows were plasma cleaned using a plasma cleaner (Harrick, Ithaca, NY, USA) for five minutes on each side with high RF power setting to remove any surface contaminants. A custom-built Teflon sample cell was used for the vSFG experiments to probe the solid-liquid interface in the external geometry where the angles of incidence are below the critical angle for total internal reflection (FIG S1).

The sum frequency generation spectra were obtained using a commercial scanning picosecond SFG spectrometer (EKSPLA, Lithuania) setup with a 532.1 nm visible beam and tunable infrared (IR) beam. Both beams were overlapped spatially and temporally at the sample surface with angles of incidence of 65° and 55° for the visible and the IR beam, respectively, at the air/alumina interface. The SFG spectra were normalized by the power of the incident beams measured simultaneously at each step scan. The SFG spectra presented here were collected using the SSP and PPP polarization combinations, where each letter signifies the polarization state of the sum frequency signal, visible, and IR beam, respectively. The S-polarized beam has the incident electric field perpendicular to the incident plane, whereas the P-polarized beam has the optical field parallel to the incident plane.

b. Temple University

CH₃CN (HPLC Grade, Fisher Chemicals Inc.), H₂O (deionized water source >18.2 MΩ·cm resistivity, Thermoscientific Barnstead Easypure II purification system equipped with a UV lamp), D₂O (Deuterium oxide (D, 99.9%), Cambridge Isotopes, USA) and a c-cut Al₂O₃ equilateral roof prism (Al₂O₃(0001)) (Team Photon Inc., San Diego, CA) were used for the experiments. The prism was cleaned using Piranha solution (1:3, H₂O₂: H₂SO₄) (CAUTION: “Piranha is extremely reactive and can cause severe damage to skin/eyes. Handle using gloves, goggles, a lab coat, and extreme care) for ~60 minutes in a Teflon dish and was rinsed with deionized water (>18.2 MΩ·cm resistivity, Thermoscientific Barnstead Easypure II purification system with UV lamp), to remove residual piranha. Then, the sample was dried using ultra-high purity N₂ gas. At the end of the cleaning process, the homemade sample holder, Teflon spacer and the prism were plasma cleaned (low-pressure RF plasma: Harrick PDC-32G) for ~2 minutes.

The vibrational sum frequency generation (vSFG) experiment was performed using a tunable broadband IR beam and a narrowband visible beam. 10% of Ti:Sapphire regenerative amplifier laser system (Coherent, Libra-F-1K-110-HE+), generating 5 mJ pulses at 800 nm with 1 kHz repetition rate and 120 fs pulse duration, after passing through a bandpass filter (~2 nm, 800 nm, CVI Laser Optics), was used as a visible beam of ~30 μJ. Approximately, 90% of the Libra output pumps a commercial optical amplifier (OPA: Coherent, TOPAS-Prime HE) to generate a tunable mid-IR pulse in the 2-5 μm spectral region using external difference frequency generation (DFG) in an AgGaS₂ crystal. Both the visible (200 mm focal length lens) and IR (50 mm focal length lens) beams were spatially and temporally overlapped at the sample interface to generate sum frequency (SF) light. The incident angles at the interface were 60°: IR ~10 μJ/pulse and 54°:

Visible $\sim 10 \mu\text{J}/\text{pulse}$ with ~ 75 and $200 \mu\text{m}$ spot size, respectively. The angles of incidence were above the critical angle for $\alpha\text{-Al}_2\text{O}_3(0001)/\text{water}$ interface to reach Fresnel factor enhancement at total internal reflection (TIR) geometry. The resulting vSFG response was separated from the 800 nm visible beam using a 750 nm short-pass filter (Thorlabs) and collected via a liquid nitrogen cooled ($-120 \text{ }^\circ\text{C}$) charge-coupled device detector array (Princeton instrument) coupled to a spectrograph (300i Acton Research Corp.)

The non-resonant response of a gold-coated ($\sim 100 \text{ nm}$ thick) $\alpha\text{-Al}_2\text{O}_3(0001)$ (Team Photon Inc., San Diego, CA, $15 \text{ mm} \times 13 \text{ mm} \times 15 \text{ mm}$) was collected under the PPP polarization configuration for vSFG normalization. After this, the sample spectra were collected in PPP and SSP polarization configurations and then normalized with the spectrum collected from a gold-coated $\alpha\text{-Al}_2\text{O}_3(0001)$ surface.

II. Experimental geometries:

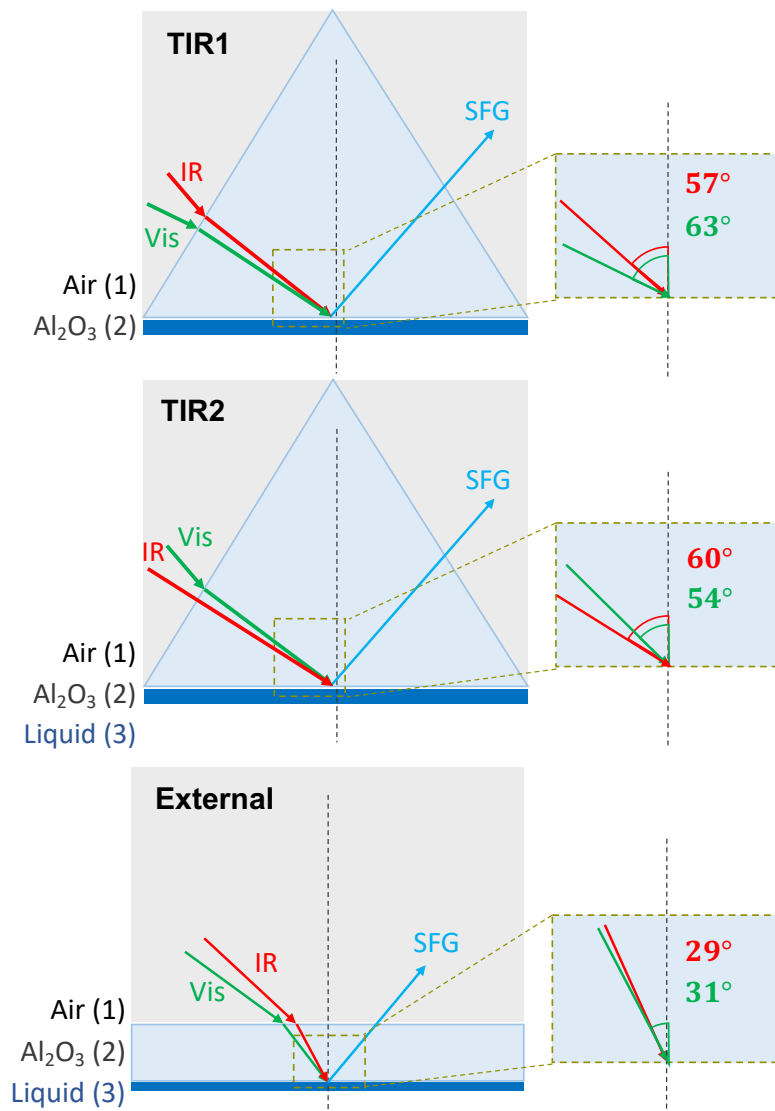


FIG S1: Experimental geometries A) TIR1 geometry vSFG setup at $\alpha\text{-Al}_2\text{O}_3(0001)/\text{liquid}$ prism: $\theta_{\text{Vis}} \approx 63^\circ$, $\theta_{\text{IR}} \approx 57^\circ$, B) TIR2 geometry vSFG setup at $\alpha\text{-Al}_2\text{O}_3(0001)/\text{liquid}$ prism: $\theta_{\text{Vis}} \approx 54^\circ$, $\theta_{\text{IR}} \approx 60^\circ$, C) External geometry vSFG setup at liquid/ $\alpha\text{-Al}_2\text{O}_3(0001)$ window: $\theta_{\text{Vis}} \approx 31^\circ$, $\theta_{\text{IR}} \approx 29^\circ$.

III. Approaches for deriving the interfacial dielectric constant:

a. The slab model

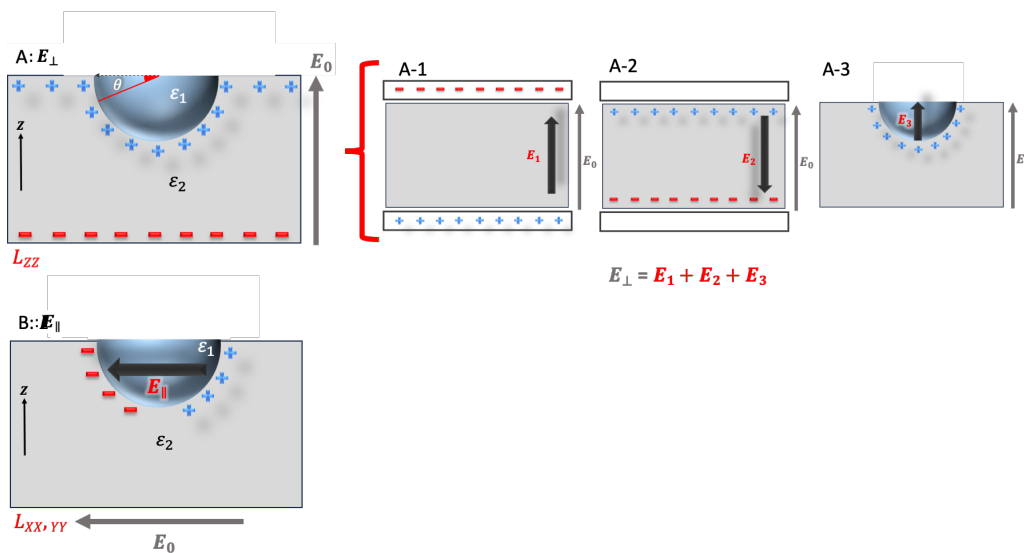


FIG S2: Schematic representation of the resulting electric fields for the slab model for a hemisphere inside a block of a dielectric between the plates of a parallel plate capacitor subjected to an external field along A) the Z-axis (Perpendicular, E_{\perp}) and B) the X or Y-axis (Parallel, E_{\parallel}). In case A, the induced field acting on the hemisphere is composed of the components E_1 (A-1), E_2 (A-2), and E_3 (A-3), along the Z-axis. The thick black arrows inside the figures represent the direction of the induced electric field components. The angle θ shown in B is the schematic representation of the angle used in equation S3.

Induced electric field along the Z-axis: (Perpendicular, E_{\perp})

To describe the induced electric field along the Z-axis, we considered a block of dielectric (FIG S2 A-1 - A-3: gray box), between the plates of a parallel plate capacitor, polarized by an external electric field (E_0) and contains a hemisphere (representing the interfacial molecules with half solvated shells) of different dielectric constant [1]. In this configuration, the induced electric field along the Z-axis (FIG S2A) can be divided into three distinct components considering Gauss's law for a dielectric medium:

E_1 (Equation S1, FIG S2 A-1) represents the field due to the charge density on the dielectric plates within the finite interfacial region on the parallel plate capacitor [1].

$$E_1 = \frac{D}{\epsilon_0} \quad \text{and} \quad D = P + \epsilon_0 E_0 \quad \text{then:} \quad E_1 = \frac{P + \epsilon_0 E_0}{\epsilon_0} = E_0 + \frac{P}{\epsilon_0} \quad (\text{S1})$$

E_2 (Equation S2, FIG S2 A-2) describes the field due to the charge density induced on the two sides of the dielectric plates in response to E_1 .

$$E_2 = -\frac{P}{\epsilon_0} \quad (\text{S2})$$

E_3 (Equation S3, FIG S2 A-3) represents the field due to polarization charges on the surface of the hemisphere induced by an external electric field [1].

$$E_3 = \int dE_3 = \frac{-P}{4\epsilon_0} \int_0^\pi \cos^2 \theta \sin \theta \, d\theta$$

$$\text{if } z = \text{Cos}\theta \quad \text{then:} \quad dz = -\sin\theta d\theta$$

θ represents the polar angle relative to the polarization direction as shown in FIG S2B.

$$E_3 = \int dE_3 = \frac{P}{4\epsilon_0} \int_1^{-1} z^2 dz = \frac{P}{4\epsilon_0} \left[\frac{z^3}{3} \right]_1^{-1} = \frac{P}{6\epsilon_0}$$

$$\text{Hence:} \quad E_3 = \frac{P}{6\epsilon_0} \quad (\text{S3})$$

$$E_\perp = E_1 + E_2 + E_3 = E_0 + \frac{P}{\epsilon_0} - \frac{P}{\epsilon_0} + \frac{P}{6\epsilon_0}$$

We should note that the induced polarization at the surface of the hemisphere will result from the combination of two polarizations with opposite signs due to the difference in permittivity ($\epsilon_2 \neq \epsilon_1$). The internal field which yield an opposite polarization can be calculated by $4\pi P/6$, for a hemisphere using the internal field for non-polar dielectrics [1]. Then we can define $P_1 = (\epsilon_1 - 1) E_0$.

Thus: $P = \sum P_i = P_2 - P_1 = \sum E_0 \varepsilon_0 [(\varepsilon_i - 1)] = E_0 \varepsilon_0 [(\varepsilon_2 - 1) - (\varepsilon_1 - 1)]$ then:

$$E_{\perp} = E_0 + \frac{E_0 \varepsilon_0 (\varepsilon_2 - \varepsilon_1)}{6 \varepsilon_0} = E_0 \left(\frac{\varepsilon_2 - \varepsilon_1 + 6}{6} \right) \quad (\text{S4})$$

In equations S1-S4, the E_i represent the electric fields, D stands for the electric displacement, P denotes the polarization, and ε_0 , ε_1 and ε_2 correspond to the dielectric functions in the vacuum, medium 1, and medium 2, respectively.

Parallel electric field along the XX and YY axes: (E_{\parallel}):

To calculate the parallel electric field one may use a dielectric sphere (ε_2) in an infinite dielectric (ε_1) of different dielectric constant [1]. Outside the sphere, without free charge, the potential is going to satisfy the Laplace's equation ($\nabla^2 \varphi = 0$) when an external electric field $E_{external}$ has been applied. The analysis involves the utilization of the Laplace equation to compute the electric field both outside (φ_1) and inside (φ_2) the hemisphere as follows [1]:

$$\varphi_1 = \sum_{n=0}^{\infty} \left(A_n r^n + \frac{B_n}{r^{n+1}} \right) P_n(\cos\theta) \quad (\text{S5})$$

$$\varphi_2 = \sum_{n=0}^{\infty} \left(C_n r^n + \frac{D_n}{r^{n+1}} \right) P_n(\cos\theta) \quad (\text{S6})$$

Where the $P_n(\cos\theta)$ is the spherical harmonics function. When considering the locality, continuity and non-singularity of the electric potential, we can get:

$$\varphi_1|_{r \rightarrow \infty} = -E_{external} r \cos\theta \quad (\text{S7-1})$$

$$\varphi_2|_{r \rightarrow 0} = \text{constant (nonsingular)} \quad (\text{S7-2})$$

$$\varepsilon_2 \frac{\partial \varphi_1}{\partial x} \Big|_{r \rightarrow a} = \varepsilon_1 \frac{\partial \varphi_2}{\partial x} \Big|_{r \rightarrow a} \quad (\text{S7-3})$$

$$\varphi_1|_{r \rightarrow a} = \varphi_2|_{r \rightarrow a} \quad (\text{S7-4})$$

Where a is the radius of the molecular cavity in Lorentz model, and ε_1 and ε_2 are the dielectric constant for medium 1 (hemisphere) and medium 2 (plate), respectively. It is easy to get $B_n = 0$ and $C_n = 0$ when $n \neq 1$ and the solution can be given as:

$$\varphi_1 = \left(\frac{\varepsilon_2 - \varepsilon_1}{2\varepsilon_1 + \varepsilon_2} \frac{a^3}{r^3} - 1 \right) E_{external} r \cos\theta \quad (S8-1)$$

$$\varphi_2 = - \left(\frac{3\varepsilon_1}{2\varepsilon_1 + \varepsilon_2} \right) E_{external} r \cos\theta \quad (S8-2)$$

If we ignore the contribution from the driving electric field $-E_{external} r \cos\theta$, then we can get the electric potential generated by surface bounded charge of polarized medium.

$$\varphi'_1 = \left(\frac{\varepsilon_2 - \varepsilon_1}{2\varepsilon_1 + \varepsilon_2} \frac{a^3}{r^3} \right) E_{external} r \cos\theta \quad (S9-1)$$

$$\varphi'_2 = - \left(\frac{\varepsilon_1 - \varepsilon_2}{2\varepsilon_1 + \varepsilon_2} \right) E_{external} r \cos\theta \quad (S9-2)$$

Then the electric field generated by surface bounded charge (E_0 and E_0') can be given as:

$$E_{inside} = -\nabla\varphi_2 = \frac{3\varepsilon_1}{2\varepsilon_1 + \varepsilon_2} E_{external} \quad (S10-1)e$$

$$E_{outside}' = -\nabla\varphi'_1 = -\nabla\varphi'_2 = \frac{\varepsilon_2 - \varepsilon_1}{2\varepsilon_2 + \varepsilon_1} E_{external} \quad (S10-2)$$

In this scenario we consider the $E_{external} = E_{\parallel}$ and $E_{inside} = E_0$ as a driving force for the induced polarization outside the hemisphere (FIG S2 B).

$$E_{\parallel} = E_0 \left(\frac{2\varepsilon_2 + \varepsilon_1}{3\varepsilon_2} \right) \quad (S11)$$

Considering this scenario the induced electric field is described with similar approach to Shen et.al while considering $\varepsilon_1 = 1$ the parallel electric field will reduce to the $E_{\parallel} = E_0 \left(\frac{2\varepsilon_2 + 1}{3\varepsilon_2} \right)$ [2].

The perpendicular (E_{\perp} : FIG S2A) and parallel (E_{\parallel} : FIG S2B) and electric field components (as explained above along the X or Y-axis and the Z-axis, respectively) at the interface can be determined using the Fresnel equations (equations S12-1 – S12-3) [3].

$$L_{XX}(\omega_I) = \frac{2\varepsilon_1(\omega_I) \cos \gamma_I}{\varepsilon_1(\omega_I) \cos \gamma_I + \varepsilon_2(\omega_I) \cos \theta_I} \quad (\text{S12} - 1)$$

$$L_{YY}(\omega_I) = \frac{2\varepsilon_1(\omega_I) \cos \theta_I}{\varepsilon_1(\omega_I) \cos \theta_I + \varepsilon_2(\omega_I) \cos \gamma_I} \quad (\text{S12} - 2)$$

$$L_{ZZ}(\omega_I) = \frac{2\varepsilon_2(\omega_I) \cos \theta_I}{\varepsilon_1(\omega_I) \cos \gamma_I + \varepsilon_2(\omega_I) \cos \theta_I} \frac{\varepsilon_1(\omega_I)}{\varepsilon'(\omega_I)} \quad (\text{S12} - 3)$$

Knowing that $L_{ZZ}/L_{YY} = \varepsilon_1/\varepsilon'$, $L_{XX} = L_{YY} = E_{\perp}/E_0$ and $L_{ZZ} = E_{\parallel}/E_0$ we have [2]:

$$\frac{L_{ZZ}}{L_{XX} \text{ or } L_{YY}} = \frac{E_{\parallel}}{E_{\perp}} = \frac{\varepsilon_1}{\varepsilon'} = \frac{\left(\frac{2\varepsilon_2+\varepsilon_1}{3\varepsilon_2}\right)}{\left(\frac{\varepsilon_2-\varepsilon_1+6}{6}\right)} = \frac{2(2\varepsilon_2+\varepsilon_1)}{\varepsilon_2(\varepsilon_2-\varepsilon_1+6)} \quad (\text{S13})$$

Thus, by simplifying and reordering equation S13 we would have:

$$\varepsilon' = \frac{\varepsilon_1 \varepsilon_2 (\varepsilon_2 - \varepsilon_1 + 6)}{2(2\varepsilon_2 + \varepsilon_1)} \quad (\text{S14})$$

knowing $n = \sqrt{\varepsilon}$

$$n' = \sqrt{\frac{n_1^2 n_2^2 (n_2^2 - n_1^2 + 6)}{2(2n_2^2 + n_1^2)}} \quad (\text{S15})$$

b. The Lorentz model

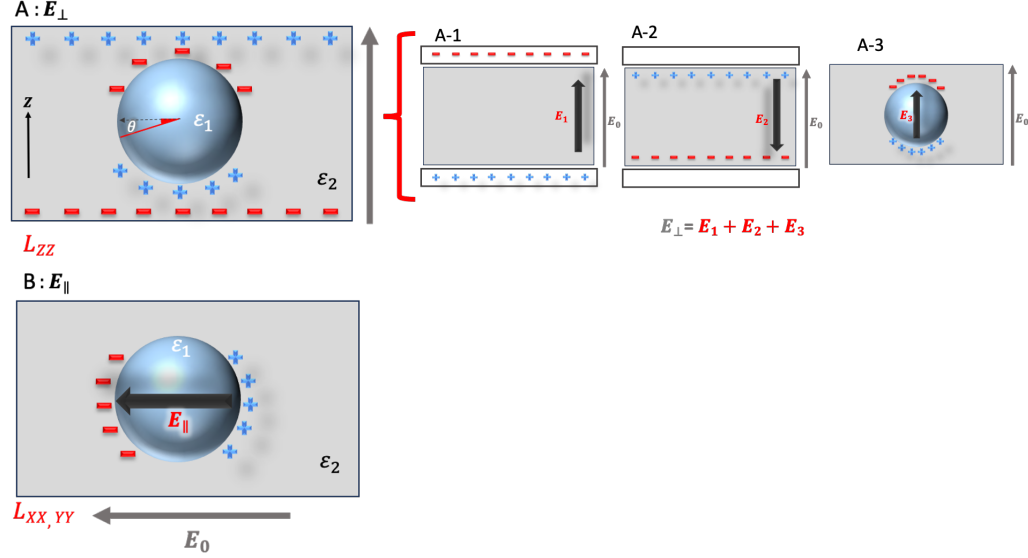


FIG S3: Schematic representation of the resulting electric fields for the Lorentz model for a sphere inside block of dielectric between the plates of a parallel plate capacitor subjected to an external field along A) the Z-axis (Perpendicular, E_{\perp}) and B) the X or Y-axis (Parallel, E_{\parallel}). In case A, the induced field acting on the sphere is composed of the components E_1 (A-1), E_2 (A-2), and E_3 (A-3), along the Z-axis. The thick black arrows inside the figures represent the direction of the induced electric field components. The angle θ shown in B is the schematic representation of the angle used in the equation S18.

Electric field along the Z-axis: (Perpendicular, E_{\perp})

Unlike the half-solvated sphere, here the entire sphere is immersed in the dielectric medium and is considered fully solvated. In this configuration, similar to the hemisphere approach, the induced electric field along the Z-axis comprises three distinct components:

E_1 (Equation S16, FIG S3 A-1) characterizes the field arising from the charge density on the dielectric plates within the finite interfacial area on the parallel plate capacitor.

$$E_1 = \frac{D}{\epsilon_0} \quad \text{and} \quad D = P + \epsilon_0 E_0 \quad \text{then:} \quad E_1 = \frac{P + \epsilon_0 E_0}{\epsilon_0} = E_0 + \frac{P}{\epsilon_0} \quad (\text{S16})$$

E_2 (Equation 17, FIG S3 A-2) represents the field resulting from the charge density induced on both sides of the dielectric plates due to E_1 .

$$E_2 = -\frac{P}{\varepsilon_0} \quad (\text{S17})$$

E_3 (Equation S18, FIG S3 A-3) represents the field intensity due induced polarization charges on the surface of the sphere by an external electric field.

$$E_3 = \int dE_3 = \frac{-P}{2\varepsilon_0} \int_0^\pi \cos^2\theta \sin\theta d\theta, \text{ if } z = \text{Cos}\theta; \text{ Then } dz = -\sin\theta d\theta$$

$$E_3 = \int dE_3 = \frac{-P}{2\varepsilon_0} \int_0^\pi \cos^2\theta \sin\theta d\theta$$

$$\text{if } z = \text{Cos}\theta \quad \text{then: } dz = -\sin\theta d\theta$$

θ represents the polar angle relative to the polarization direction as shown in FIG S2B.

$$E_3 = \int dE_3 = \frac{P}{2\varepsilon_0} \int_1^{-1} z^2 dz = \frac{P}{42} \left[\frac{z^3}{3} \right]_1^{-1} = \frac{P}{2\varepsilon_0}$$

$$\text{Hence: } E_3 = \frac{P}{3\varepsilon_0} \quad (\text{S18})$$

$$E_\perp = E_1 + E_2 + E_3 = E_0 + \frac{P}{\varepsilon_0} - \frac{P}{\varepsilon_0} + \frac{P}{3\varepsilon_0}$$

Knowing that $P = E_0 \varepsilon_0 [(\varepsilon_i - 1)]$ and similar to the scenario we explained above then:

$$E_\perp = E_0 + \frac{E_0 \varepsilon_0 (\varepsilon_2 - \varepsilon_1)}{3\varepsilon_0} = E_0 \left(\frac{\varepsilon_2 - \varepsilon_1 + 3}{3} \right) \quad (\text{S19})$$

Electric field along the XX or YY-axis: (Parallel, E_\parallel):

For a dielectric sphere in a dielectric, the electric field is described as [1]:

$$E_\parallel = E_0 \left(\frac{2\varepsilon_2 + \varepsilon_1}{3\varepsilon_2} \right) \quad (\text{S20})$$

By calculating the perpendicular (E_{\perp}) (equation S20: Figure S3A) and parallel (E_{\parallel}) (equation S19: Figure S3B) induced electric field components at the interface using the Fresnel equation (equations S12-1 – S12-3) [3] and knowing that $L_{ZZ}/L_{YY} = \varepsilon_1/\varepsilon'$, $L_{XX} = L_{YY} = E_{\perp}/E_0$ and $L_{ZZ} = E_{\parallel}/E_0$ [2]:

$$\frac{L_{ZZ}}{L_{XX} \text{ or } L_{YY}} = \frac{E_{\parallel}}{E_{\perp}} = \frac{\varepsilon_1}{\varepsilon'} = \frac{\left(\frac{2\varepsilon_2+\varepsilon_1}{3\varepsilon_2}\right)}{\left(\frac{\varepsilon_2-\varepsilon_1+3}{3}\right)} = \frac{(2\varepsilon_2+\varepsilon_1)}{\varepsilon_2(\varepsilon_2-\varepsilon_1+3)} \quad (\text{S21})$$

$$\varepsilon' = \frac{\varepsilon_1\varepsilon_2(\varepsilon_2-\varepsilon_1+3)}{(2\varepsilon_2+\varepsilon_1)} \quad (\text{S22})$$

knowing $n = \sqrt{\varepsilon}$

$$n' = \sqrt{\frac{n_1^2 n_2^2 (n_2^2 - n_1^2 + 3)}{(2n_2^2 + n_1^2)}} \quad (\text{S23})$$

IV. Comparison of expressions derived using the slab model (III-a) vs. Lorentz model (III-b):

We derived expressions for the interfacial dielectric constant using the slab model (section III-a) and Lorentz model (section III-b). Then, we compared the experimentally measured frequency-dependent $\left|\chi_{eff,PPP}^{(2)}\right|^2$ ratio ($\left|\chi_{eff,PPP}^{(2)}\right|^2 (TIR2)/\left|\chi_{eff,PPP}^{(2)}\right|^2 (Ext)$ and $\left|\chi_{eff,PPP}^{(2)}\right|^2 (TIR1)/\left|\chi_{eff,PPP}^{(2)}\right|^2 (Ext)$) for two different geometries with the calculated ratios from both models, described in section IV. The expression derived for the interfacial dielectric constant (ε') using the slab model (Fig 4A) aligns more closely with the experimental data for the OH stretch of H₂O (Manuscript: Fig 2D) compared to the Lorentz model (Fig S4 B) at the interface. In contrast, the prediction of the Lorentz model (equation S22) deviates from experimental data.

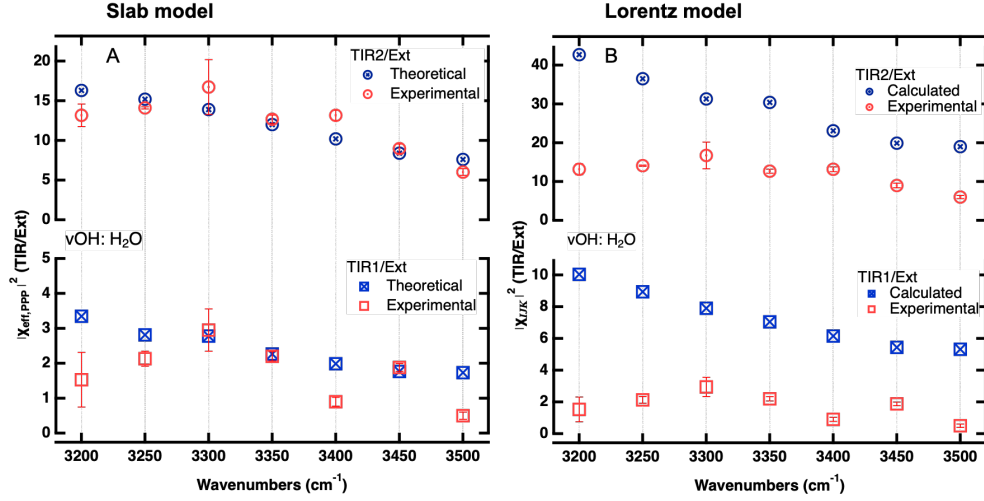


FIG S4: Calculated frequency dependent $|\chi_{eff,PPP}^{(2)}|^2$ ratio of the TIR 2: Top, 1: Bottom with respect to the external geometry in the OH stretch region of the $\text{H}_2\text{O}/\text{Al}_2\text{O}_3$ interface for A) Slab model and B) Lorentz model at the interface.

V. Critical angles:

The critical angle is defined as the angle of incidence beyond which total internal reflection occurs. This happens when light travels from a medium with a higher refractive index towards one with a lower refractive index. The calculation of the critical angle (Table S1) is governed by Snell's law using the formula $\theta_c = \arcsin(n_2/n_1)$, where θ_c is the critical angle, n_1 is the refractive index of the denser medium, and n_2 is the refractive index of the less dense medium. This phenomenon is only observable when n_1 exceeds n_2 .

Table S1: Refractive indices of α -Al₂O₃(0001), H₂O, D₂O and CH₃CN and the critical angles at the respective solid-liquid interfaces.

Wavelength	Refractive indices				Critical angle		
	Al ₂ O ₃ [4]	H ₂ O [5]	D ₂ O [5]	CH ₃ CN [6]	H ₂ O /Al ₂ O ₃	D ₂ O /Al ₂ O	CH ₃ CN/ Al ₂ O ₃
SFG: 633 nm H ₂ O	1.76	1.33	-	-	49.08°	-	-
SFG:597 nm D ₂ O		-	1.33	-	-	49.08°	-
SFG: 678 nm CH ₃ CN		-	-	1.34	-	-	49.58°
Vis: 800 nm	1.76	1.33	1.33	1.33	49.08°	49.08°	49.08°
SFG:452 nm H ₂ O	1.77	1.33	-	-	49.08°	-	-
SFG: 473 nm D ₂ O		-	1.33	-	-	48.71°	-
SFG:472 nm CH ₃ CN		-	-	1.34	-	-	49.21°
Vis: 532 nm	1.77	1.33	1.33	1.34	48.71°	48.71°	49.21°
IR: 3030 nm; (3300 cm ⁻¹)	1.71	1.40+i0.25	-	-	56.14°	-	-
IR: 4255 nm; (2350 cm ⁻¹)	1.66	-	1.43+i0.20	-	-	60.17°	-
IR: 4444 nm; (2250 cm ⁻¹)	1.65	-	-	1.34+i0.05	-	-	54.30°

VI. Angular dependent effective nonlinear susceptibility $|\chi_{eff,PPP}^{(2)}|^2$ of the TIR2 and TIR1 and the external geometry with constant IR angle:

Defining the interfacial dielectric constant using slab model?

We hypothesized that by varying the angles of incidence of the visible and IR beams one can determine ϵ' by comparing the calculated $|\chi_{eff}^{(2)}|^2$ (equation 1) with experimental values of $|\chi_{eff}^{(2)}|^2$. We used different theoretical models, Table S1, in addition to the expression we derived above using the slab model (G) for ϵ' . Two of the models are derived from established formulas

and prediction (C, E and F) [2,7,8] while the other models (A-D) are utilized for comparative purposes.

Table S2: Seven proposed formulas for the dielectric constant at a buried interface.

Model	Interfacial dielectric constant
A	ϵ_1
B	ϵ_2
C [8]	$(0.5\sqrt{\epsilon_1} + 0.5\sqrt{\epsilon_2})^2$
D	$(0.4\sqrt{\epsilon_1} + 0.6\sqrt{\epsilon_2})^2$
E [7]	$(0.2\sqrt{\epsilon_1} + 0.8\sqrt{\epsilon_2})^2$
F [2]	$\epsilon^* = \epsilon_2(\epsilon_2 + 5)/(4\epsilon_2 + 2)$
G	$\epsilon' = \epsilon_1\epsilon_2(\epsilon_2 - \epsilon_1 + 6)/2(2\epsilon_2 + \epsilon_1)$

The angular dependence of $|\chi_{eff}^{(2)}|^2$ (Equations 4a-4d) was calculated using the dielectric constants of the solid (ϵ_1 : α -Al₂O₃) and the liquid (ϵ_2 : H₂O, D₂O and CH₃CN) phases, while varying the angles of incidence of the visible beam and keeping the angle of the incident for the IR beam constant. As χ_{PPP} contains several χ_{ijk} , we simplify the analysis by assuming $\chi_{XXZ} = \chi_{XZX} = \chi_{ZXX} = \chi_{ZZZ} = 1$ (Equation 2d). Without knowing the actual values of χ_{ijk} this is a reasonable first approximation.

To compare the different expression for the interfacial dielectric constant, A-G (Table S2), we calculated the angular dependence of $|\chi_{eff}^{(2)}|^2$ in the OH stretch region (~ 3350 cm⁻¹) for the α -Al₂O₃/ H₂O interface (FIG S5), the OD stretch region for the α -Al₂O₃/D₂O interface (FIG S6), in the CH stretch for the α -Al₂O₃/CH₃CN interface (FIG S7), and in the C \equiv N stretch region for the

α -Al₂O₃/CH₃CN interface (FIG S8). The calculation of angle dependant effective nonlinear susceptibility components in the TIR2 geometry for the PPP polarization, FIG S5-S8, using different models for the interfacial dielectric constant, reveals a notable dependence of $\left|\chi_{eff,PPP}^{(2)}\right|^2$ on the selected ϵ' model. When $\epsilon' \approx \epsilon_2$ (dielectric constant of the liquid) $\left|\chi_{eff,PPP}^{(2)}\right|^2$ has a higher intensity unlike the $\epsilon^* = \epsilon_2(\epsilon_2 + 5)/(4\epsilon_2 + 2)$ where $\left|\chi_{eff,PPP}^{(2)}\right|^2$ has the lowest value for a given angle at TIR1, TIR2 and Ext. geometies (FIG S5-S8: Angles are highlighted by gray lines). These results (FIG S5-S8) show that the magnitude of $\left|\chi_{eff,PPP}^{(2)}\right|^2$ response is influenced by ϵ' , highlighting the significance of the contribution of interfacial dielectric constant.

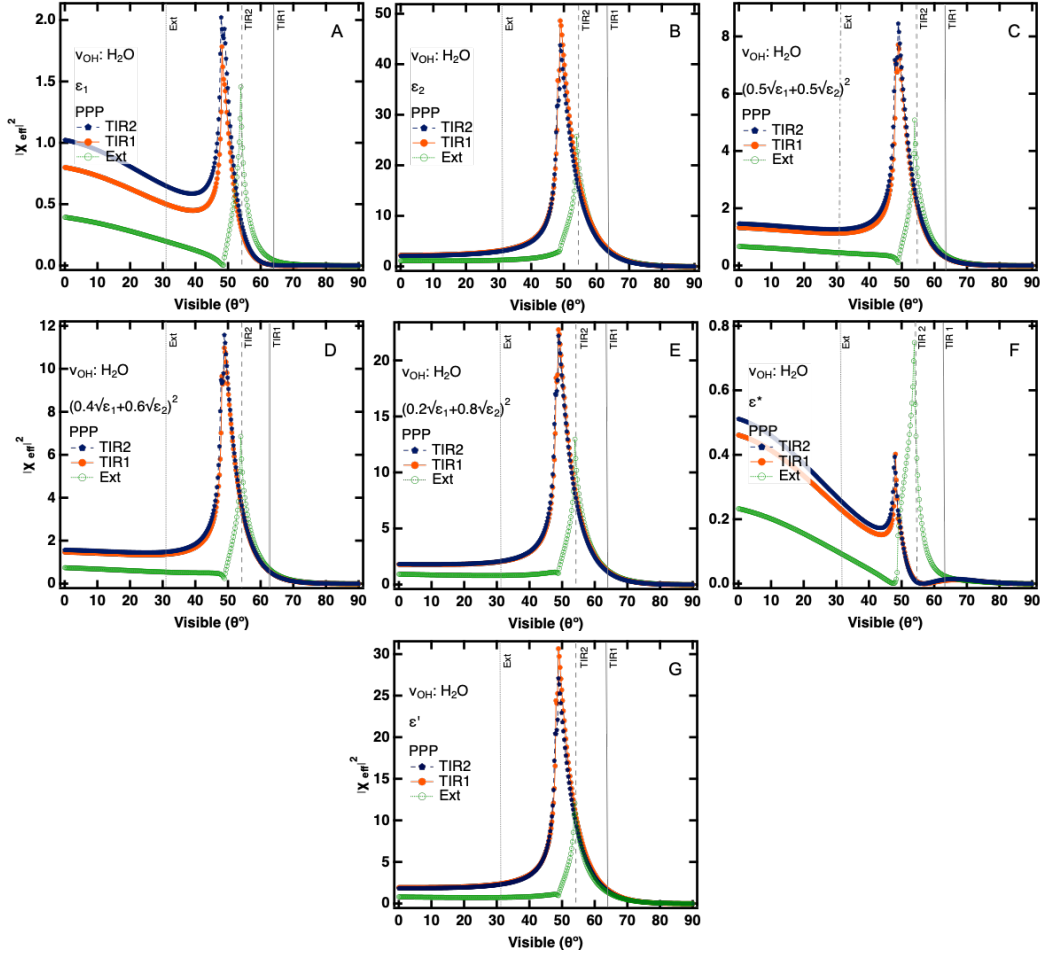


FIG S5: Angular dependence of the effective nonlinear susceptibility $|\chi_{eff,PPP}^{(2)}|^2$ in TIR2 (dark blue), TIR1 (orange) and external (green) geometry in the OH stretch region of the α -Al₂O₃/H₂O interface. Seven different models for ϵ' including ϵ_1 , ϵ_2 , $(0.5\sqrt{\epsilon_1} + 0.5\sqrt{\epsilon_2})^2$, $(0.4\sqrt{\epsilon_1} + 0.6\sqrt{\epsilon_2})^2$, $(0.2\sqrt{\epsilon_1} + 0.8\sqrt{\epsilon_2})^2$, $\epsilon^* = \epsilon_2(\epsilon_2 + 5)/(4\epsilon_2 + 2)$ and $\epsilon' = \epsilon_1\epsilon_2(\epsilon_2 - \epsilon_1 + 6)/2(2\epsilon_2 + \epsilon_1)$ where ϵ_1 and ϵ_2 are the dielectric constants of the solid and liquid phases, respectively. Gray dotted lines represent the corresponding visible angles for the TIR2 (54°), TIR1 (63°) and external (31°) geometries.

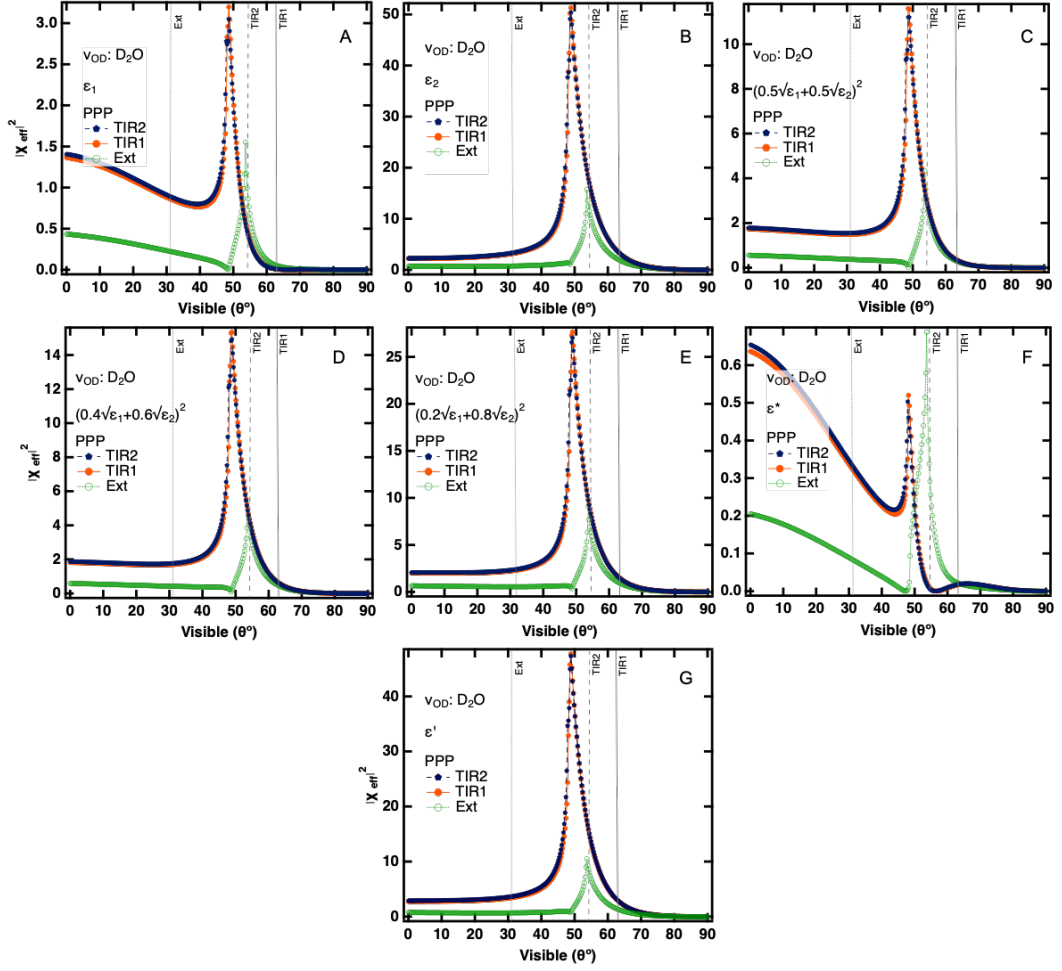


FIG S6: Angular dependence of the effective nonlinear susceptibility $|\chi_{\text{eff,PPP}}^{(2)}|^2$ in TIR2 (dark blue), TIR1 (orange) and external (green) geometry in the C \equiv N stretch of the α -Al $_2$ O $_3$ /CH $_3$ CN interface. Seven different models for ϵ' including ϵ_1 , ϵ_2 , $(0.5\sqrt{\epsilon_1} + 0.5\sqrt{\epsilon_2})^2$, $(0.4\sqrt{\epsilon_1} + 0.6\sqrt{\epsilon_2})^2$, $(0.2\sqrt{\epsilon_1} + 0.8\sqrt{\epsilon_2})^2$, $\epsilon^* = \epsilon_2(\epsilon_2 + 5)/(4\epsilon_2 + 2)$ and $\epsilon' = \epsilon_1\epsilon_2(\epsilon_2 - \epsilon_1 + 6)/2(2\epsilon_2 + \epsilon_1)$ where ϵ_1 and ϵ_2 are the dielectric constants of the solid and liquid phases, respectively. Gray dotted lines represent the corresponding visible angles for the TIR2 (54 $^\circ$), TIR1 (63 $^\circ$) and external (31 $^\circ$) geometries.

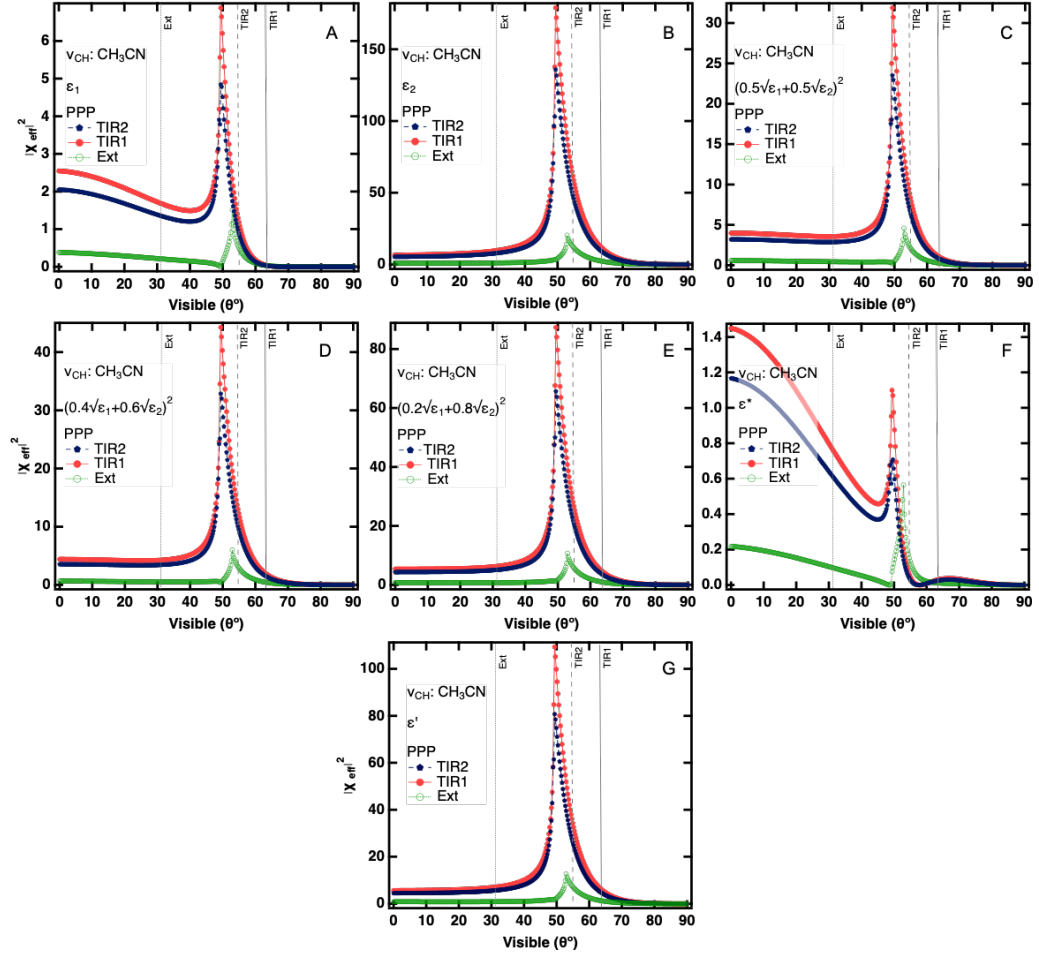


FIG S7: Angular dependence of the effective nonlinear susceptibility $|\chi_{eff,PPP}^{(2)}|^2$ in TIR2 (dark blue), TIR1 (orange) and external (green) geometry in the CH stretch of the α -Al₂O₃/CH₃CN interface. Seven different models for ϵ' including ϵ_1 , ϵ_2 , $(0.5\sqrt{\epsilon_1} + 0.5\sqrt{\epsilon_2})^2$, $(0.4\sqrt{\epsilon_1} + 0.6\sqrt{\epsilon_2})^2$, $(0.2\sqrt{\epsilon_1} + 0.8\sqrt{\epsilon_2})^2$, $\epsilon^* = \epsilon_2(\epsilon_2 + 5)/(4\epsilon_2 + 2)$ and $\epsilon' = \epsilon_1\epsilon_2(\epsilon_2 - \epsilon_1 + 6)/2(2\epsilon_2 + \epsilon_1)$ where ϵ_1 and ϵ_2 are the dielectric constants of the solid and liquid phases, respectively. Gray dotted lines represent the corresponding visible angles for the TIR2 (54°), TIR1 (63°) and external (31°) geometries.

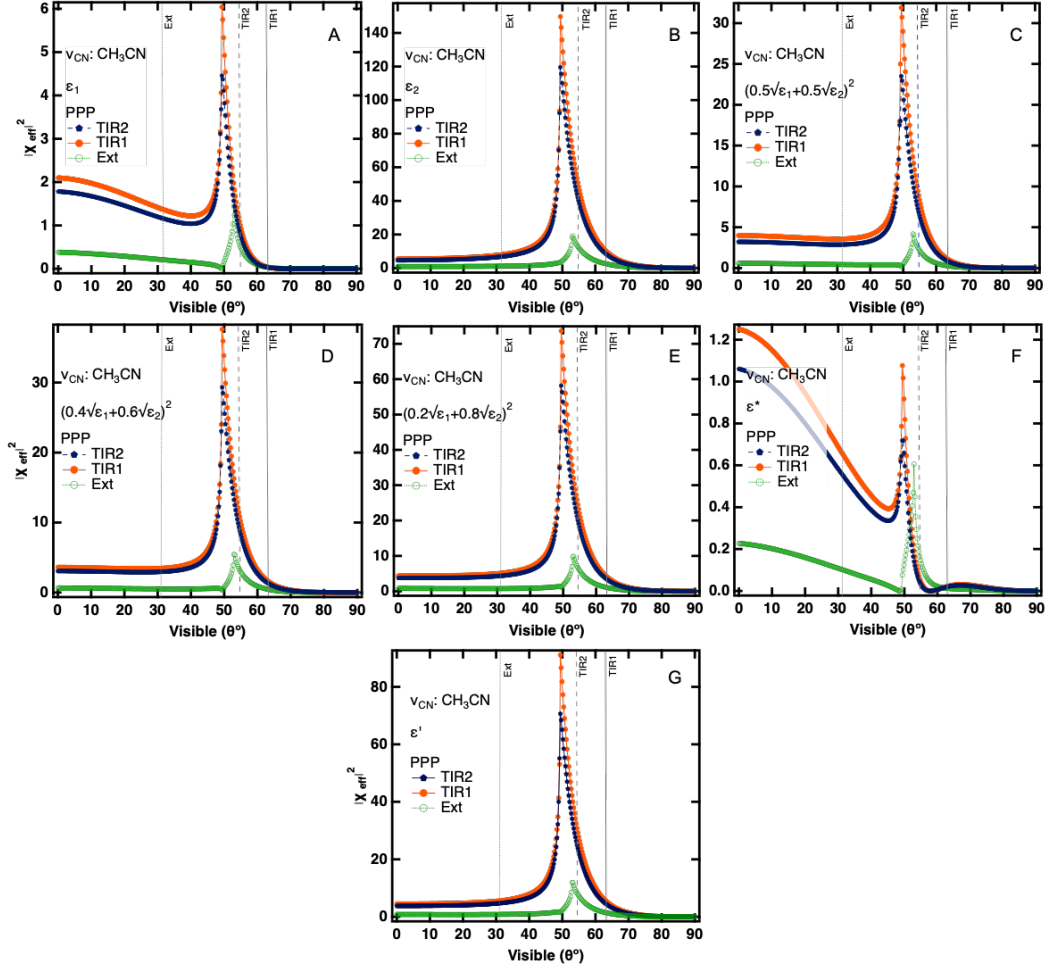


FIG S8: Angular dependence of the effective nonlinear susceptibility $|\chi_{eff,PPP}^{(2)}|^2$ in TIR2 (dark blue), TIR1 (Orange) and external (green) geometry in the OD stretch region of the α -Al₂O₃/D₂O interface. Seven different models for ϵ' including ϵ_1 , ϵ_2 , $(0.5\sqrt{\epsilon_1} + 0.5\sqrt{\epsilon_2})^2$, $(0.4\sqrt{\epsilon_1} + 0.6\sqrt{\epsilon_2})^2$, $(0.2\sqrt{\epsilon_1} + 0.8\sqrt{\epsilon_2})^2$, $\epsilon^* = \epsilon_2(\epsilon_2 + 5)/4\epsilon_2$ and $\epsilon' = \epsilon_1\epsilon_2(\epsilon_2 - \epsilon_1 + 6)/2(2\epsilon_2 + \epsilon_1)$ where ϵ_1 and ϵ_2 are the dielectric constants of the solid and liquid phases, respectively. Gray dotted lines represent the corresponding visible angles for the TIR2 (54°), TIR1 (63°) and external (31°) geometries.

VII. Which expression performs better?

We have calculated frequency dependent $\left|\chi_{eff,PPP}^{(2)}\right|^2$ using the expression derived from classical MD simulations [7], $\varepsilon' = (0.2\sqrt{\varepsilon_1} + 0.8\sqrt{\varepsilon_2})^2$, at the OH (A) and OD (B) stretch frequencies (FIG S9: A and B). Our goal was to compare the frequency dependency of $|\varepsilon'|$ using both our expression and the MD simulations.

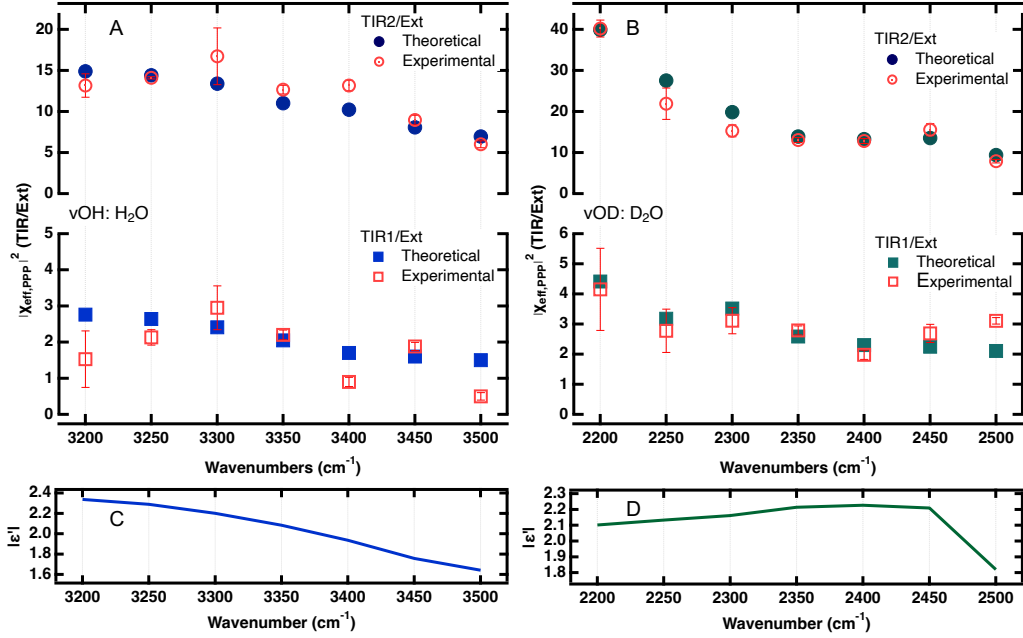


FIG S9: Calculated frequency dependent $\left|\chi_{eff,PPP}^{(2)}\right|^2$ ratio for TIR2 (Top) and TIR1 (Bottom) with respect to the external geometry for the A) OH stretch of H₂O (blue) and B) OD stretch of D₂O (green) at the α -Al₂O₃ interface compared to the experimental data (red). The frequency dependence of $|\varepsilon'|$ at the C) α -Al₂O₃/H₂O and the D) α -Al₂O₃/D₂O interfaces. The expression $\varepsilon' = (0.2\sqrt{\varepsilon_1} + 0.8\sqrt{\varepsilon_2})^2$ was used to calculate the interfacial dielectric constant.

The expressions $\varepsilon_1\varepsilon_2(\varepsilon_2 - \varepsilon_1 + 6)/2(2\varepsilon_2 + \varepsilon_1)$ and $(0.2\sqrt{\varepsilon_1} + 0.8\sqrt{\varepsilon_2})^2$ [7] for ε' both show improvement compared to the other models when we compared the experimental $\left|\chi_{eff}^{(2)}\right|^2$

ratio to the calculated ratio (FIG3). However, $\varepsilon_1 \varepsilon_2 (\varepsilon_2 - \varepsilon_1 + 6) / 2 (2\varepsilon_2 + \varepsilon_1)$ (model G) demonstrates somewhat better agreement over $(0.2\sqrt{\varepsilon_1} + 0.8\sqrt{\varepsilon_2})^2$ (model E) for the frequency dependent results in the OD and OH stretch regions of the $\text{Al}_2\text{O}_3/\text{D}_2\text{O}$ and $\text{Al}_2\text{O}_3/\text{H}_2\text{O}$ interfaces with (FIG S5 and S6). The differences between the two models could be due to the approaches; ours is predicated on continuum electrostatics, whereas the MD simulation is based on molecular-level interactions.

We quantified the accuracy of our theoretical models against experimental data using Root Mean Square Error (RMSE), equation S24, and Mean Absolute Error (MAE), equation S25, to measure deviations [9].

$$\text{RMSE} = \sqrt{\frac{1}{n} \sum_{i=1}^n (y_i - \hat{y}_i)^2} \quad (\text{S24})$$

$$\text{MAE} = \frac{1}{n} \sum_{i=1}^n |y_i - \hat{y}_i| \quad (\text{S25})$$

where the y_i are the experimental values, the \hat{y}_i are the calculated values and n is the number of observations, in our case 7 data points, i.e., 7 different frequencies for which we have refractive indices from the literature.

Model G exhibits a deviation from the experimental data, as reflected by its reduced RMSE, suggesting that the deviations in the predictions from the experimental values are generally smaller (FIG S10 and S11). Additionally, the reduced MAE of model G indicates a lower average error for the calculated values, further showing its enhanced accuracy. Conversely, model E shows elevated RMSE and MAE values, indicating a broader dispersion of prediction errors and a higher mean error, respectively. However, in general, Model G and Model E exhibit comparable precision and produce outcomes that are nearly equivalent.

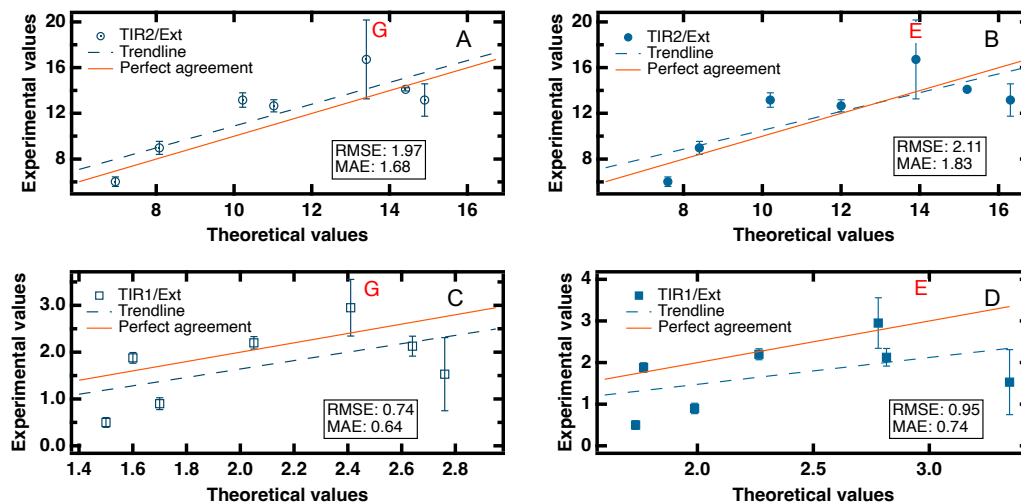


FIG S10: Comparative quantitative analysis of models G (A and C) and E (B and D) versus frequency dependent experimental data in the OH stretch region of the $\text{H}_2\text{O}/\text{Al}_2\text{O}_3$ interface based on their theoretical predictions for (TIR(1 or 2)/Ext) relative to experimental observations. The dashed lines represent the best fits to the data, while the solid lines indicate the line of perfect agreement, where theoretical values match exactly with experimental results. Data points with error bars for the experiments signify the variability within individual measurements. The error bars for have been defined using multiple experiments.

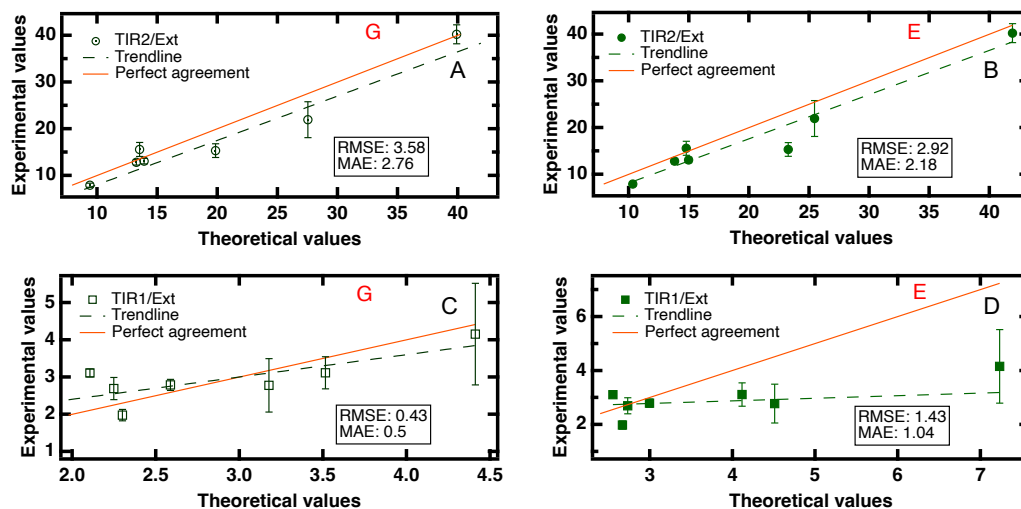


FIG S11: Comparative quantitative analysis of models G (A and C) and E (B and D) versus frequency dependent experimental data in the OD stretch region of the $\text{D}_2\text{O}/\text{Al}_2\text{O}_3$ interface based on their theoretical predictions for (TIR(1 or 2)/Ext) relative to experimental observations. The dashed lines represent the best fits to the data, while the solid lines indicate the line of perfect agreement, where theoretical values match exactly with experimental results. Data points with error bars for the experiments signify the variability within individual measurements. The error bars for have been defined using multiple experiments.

VIII. References:

- [1] C. Böttcher, *Theory of Electric Polarization* (Elsevier, 1973).
- [2] X. Zhuang, P. Miranda, D. Kim, and Y. Shen, Mapping molecular orientation and conformation at interfaces by surface nonlinear optics, *Physical Review B* **59**, 12632, (1999).
- [3] K. Shiratori and A. Morita, Molecular theory on dielectric constant at interfaces: A molecular dynamics study of the water/vapor interface, *The Journal of Chemical Physics* **134**, 234705, (2011).
- [4] A. Morita, *Theory of sum frequency generation spectroscopy* (Singapore: Springer, 2018).
- [5] C. Laurent, H. Billiet, and L. De Galan, On the use of alumina in HPLC with aqueous mobile phases at extreme pH, *Chromatographia* **17**, 253-258, (1983).
- [6] K. Moutzouris, M. Papamichael, S. C. Betsis, I. Stavrakas, G. Hloupis, and D. Triantis, Refractive, dispersive and thermo-optic properties of twelve organic solvents in the visible and near-infrared, *Applied Physics B* **116**, 617-622, (2014).
- [7] L. Wang, T. Ishiyama, and A. Morita, Theoretical investigation of C–H vibrational spectroscopy. I. Modeling of methyl and methylene groups of ethanol with different conformers, *The Journal of Physical Chemistry A* **121**, 6687-6700, (2017).
- [8] L. Wang, R. Murata, K.-i. Inoue, S. Ye, and A. Morita, Dispersion of Complex Refractive Indices for Intense Vibrational Bands. II. Implication to Sum Frequency Generation Spectroscopy, *The Journal of Physical Chemistry B* **125**, 9804-9810, (2021).
- [9] C. J. Willmott and K. Matsuura, Advantages of the mean absolute error (MAE) over the root mean square error (RMSE) in assessing average model performance, *Climate Research* **30**, 79-82, (2005).